



# Probing into the radiative mechanisms and drivers influencing urban heat-cold islands and urban pollution islands during heavy-haze events in a cold megacity of Northeast China



Stephen Dauda Yabo <sup>a,b,c,d</sup>, Lu Lu <sup>a,b,c</sup>, Lixin Ma <sup>a,b,c,e</sup>, Bo Li <sup>f</sup>, Donglei Fu <sup>g</sup>, Fan Meng <sup>a,b,c</sup>, Jinpan Jiang <sup>a,b,c</sup>, Xie Shengjin <sup>a,b,c</sup>, Wei Zhang <sup>h,\*</sup>, Hong Qi <sup>a,b,c,\*</sup>

<sup>a</sup> State Key Laboratory of Urban Water Resource and Environment, Harbin Institute of Technology, Harbin, China

<sup>b</sup> School of Environment, Harbin Institute of Technology, Harbin, China

<sup>c</sup> Heilongjiang Provincial Key Laboratory of Polar Environment and Ecosystem, Harbin, China

<sup>d</sup> Department of Geomatics, Ahmadu Bello University, Zaria, Nigeria

<sup>e</sup> College of Design and Engineering, National University of Singapore, Singapore 117576, Singapore

<sup>f</sup> School of Environmental, Tsinghua University, Beijing 100871, PR China

<sup>g</sup> College of Urban and Environmental Sciences, Peking University, Beijing 100091, China

<sup>h</sup> School of Computer Science and Technology, Harbin Institute of Technology, Harbin, China

## ARTICLE INFO

### Keywords:

Aerosol radiative effects  
Urban meteorology island  
Urban pollution island  
Numerical modeling  
Persistent-heavy-haze  
Extreme cold

## ABSTRACT

Persistent-heavy-haze (PHH) events and extreme-cold temperatures are prevalent problems confronting the Northeastern part of China (especially Harbin) during the prolonged winter season, leading to two challenging phenomena known as the urban-heat/cold-island (UHI/UCI) and urban-pollution-island (UPI) intensities (UHII/UCII and UPII) defined as the differences between urban and rural temperature/air pollution. Although UHI and UPI have been explored, the mechanisms and novel drivers (urban-stilling-island-intensity (USII), urban-dryness-island-intensity (UDII), and urban-planetary-boundary-layer-height-intensity (UPBLHI) which are by-products of wind speed (WS), relative humidity, and planetary-boundary-layer-height (PBLH), respectively; with wind direction (WD)) influencing them are still underexplored in extreme-cold regions. Using the Weather Research and Forecasting (WRF) model coupled with Chemistry (WRF-Chem), we designed the mechanisms into non-radiative-effect (NRE), direct-radiative-effect (DRE), indirect-radiative-effect (IRE), with slope-and-shading-effect (SSE) during early-winter-heavy-haze-episode (EWHHE; December 2019) and peak-winter-persistent-heavy-haze-episode (PWPHHE; January 2020). We found that the spatial distributions of the mass concentration of pollutants (e.g., PM<sub>2.5</sub>) dominated the downtown, with the IRE and SSE accounting for >200 µg/m<sup>3</sup> in both episodes. In assessing the drivers impacting UHII and UPII, the USII favors the increase of UHII and UPII in the EWHHE but lowers the UCII in PWPHHE. Moreover, the UDII and UPBLHI were weaker in PWPHHE than the EWHHE, with NO<sub>2</sub> having the highest UDII at 7.05% (SSE), 7.00% (IRE and NRE), and 6.24% (DRE); hence, revealing that PHH lowered the PBLH. Additionally, the dominant south-to-north WD impacted the UHII and UPII. Generally, low USII, UDII, and UPBLHI with WD are major contributors to PHH in the cold region. Therefore, this work provides insight into drivers for other urban areas with severe air pollution and extreme cold problems.

**Abbreviations:** PHH, Persistent-heavy-haze; UHI (UHII), urban heat island (urban heat island intensity); UCI (UCII), urban cold island (urban cold island intensity); UPI (UPII), urban pollution island (urban pollution island intensity); UMI, urban meteorology island; USII, urban stilling island intensity; UDII, urban dryness island intensity; UPBLHI, urban planetary boundary layer height intensity; NRE, non-radiative effect; DRE, direct radiative effect; IRE, indirect radiative effect; SSE, slope and shading effect; EWHHE, early winter heavy haze episode; PWPHHE, peak winter persistent heavy haze episode.

\* Corresponding authors.

E-mail addresses: [weizhang@hit.edu.cn](mailto:weizhang@hit.edu.cn) (W. Zhang), [hongqi@hit.edu.cn](mailto:hongqi@hit.edu.cn) (H. Qi).

<https://doi.org/10.1016/j.atmosres.2024.107259>

Received 23 September 2023; Received in revised form 22 December 2023; Accepted 15 January 2024

Available online 17 January 2024

0169-8095/© 2024 Published by Elsevier B.V.

## 1. Introduction

Persistent-heavy-haze (PHH) events and extreme heat or cold temperatures are prevalent problems confronting most major cities in the Northeastern part of China (similar to other cities in China) during the prolonged winter season (Cheng et al., 2022; Fu et al., 2021a; Li et al., 2023; Yabo et al., 2023), resulting into two challenging phenomena known as the urban heat-cold island (UHI/UCI) and urban pollution island (UPI) with their intensities represented as UHII/UCII and UPII, respectively. The UHI/UCI illustrates a phenomenon in which urban regions warm up (cold) more than their adjacent rural counterparts (Oke, 1982; Oke, 1995). UHI is a by-product of progressive rapid urbanization whereby natural surfaces are being altered to impervious surfaces in the urban centers contrasted to the nearby suburban and rural areas (Cui and Shi, 2012), leading to an increase in the urban surface energy budget (Chakraborty et al., 2017). Besides UHI, a second adverse land-use shift brought on a by-product of rapid urbanization, economic growth, and industrial development, which is also principally responsible for the deteriorating air quality in metropolitan areas (Ding et al., 2017; Oliver Ling et al., 2010). The variations of air pollutants (particulate matter ( $PM_{2.5}$  and  $PM_{10}$ ), sulfur dioxide ( $SO_2$ ), nitrogen dioxide ( $NO_2$ ), carbon monoxide (CO), and ozone ( $O_3$ )) between the urban and its suburban/rural counterparts introduce the concept of urban pollution island (UPI) intensity (UPII) which is a similar concept with UHI (UHII). The UPI has only lately been used to describe the onset of spatial and temporal fluctuations in pollutant concentration that can be attributed to the presence of typical urban features and activities, (Crutzen, 2004; Li et al., 2018). Comparably, UHI and UPI are not separate phenomena, and it is therefore plausible that they coexist (Crutzen, 2004). It is imperative to note that their coexistence pose a serious threat to the most populated cities globally. To improve our understanding of these two phenomena and their radiative mechanisms have been a matter of public concern.

The aerosol radiative effects (ARE) mechanisms are considered as the process whereby aerosols (e.g.,  $PM_{2.5}$ ) suspended in the air tend to alter the radiation budget by absorbing and scattering solar radiation (Chen et al., 2020; Chylek and Wong, 1995; Li, 1998) which mainly include the direct radiative effect (DRE) and indirect radiative effect (IRE) along with the slope and shading effect (SSE) that we implemented in our previous study (Yabo et al., 2023). The DRE describes the way aerosols reflect and deviate sunlight, while the IRE is a phenomenon where aerosols modify the microphysical properties of clouds, especially the abundance of cloud droplets and their operational radius, as well as the quantity of condensed-cloud granules and ice nuclei, thereby affecting the climate (Gao et al., 2016). Additionally, the SSE influences how much surface solar radiation flux depends on the slope of the terrain and allows nearby grid cells to be shadowed (Skamarock et al., 2019). Aerosols interact heavily with meteorological factors, with the planetary boundary layer (PBL) being the region where these interactions are most intense, thereby promoting the relationship between meteorological variables and air pollutants (Z. Li et al., 2017a, 2017b; Petäjä et al., 2016). ARE tends to stabilize the PBL, warm up the atmosphere, cool down the surface, and suppress the dispersion of pollutants and their contribution to  $T_{2m}$  (Li et al., 2017b; Gao et al., 2023). During the PHH stage, ARE has been discovered to have little impact on WS, with the change being unstable (Gao et al., 2023). In addition, ARE has been discovered to exacerbate the haze episode by contributing to the increase in near-surface  $PM_{2.5}$  concentration in the North-China-Plain (Wu et al., 2019). Han et al. (2020) explained that stronger ARE occurs concurrently with greater  $PM_{2.5}$  concentration, which will further impair the diffusion conditions and result in a positive feedback loop for the heavy pollution influencing UHI directly. Recently, in our study, we found that ARE had an impact on the spatial distribution of  $PM_{2.5}$ , which resulted in a mean decrease in  $T_{2m}$  and further reduced the UHII from the appreciable difference between excellent and extremely-polluted levels during winter-haze occurrences in Harbin. Despite this

contribution to the body of knowledge in the scientific community, further probing into the drivers of UHI and UPI are unique and should be keenly studied in the cold region (especially Harbin) during the PHH periods.

The novel drivers influencing the coexistence of UHI and UPI have been introduced as the urban meteorology island (UMI) by Karlický et al. (2020) as a phenomenon that differentiates the meteorological conditions of an urban area from its surrounding suburban or rural counterparts. Apart from UHI (one of the components of UMI), other urban-induced meteorological-related components forming the island-like features have resulted in the development of other new concepts by various scientists across the world. One of the concepts is the urban stilling island (USI) intensity (USII), defined as the difference in wind speed (WS) between the urban and sub-urban or rural areas (Yang et al., 2020a, 2020b). WS is one of the meteorological drivers influencing both UHII and UPII (Hou et al., 2013). The accumulation and storage of air pollutants and heat are favored by low WS, while high WS helps in diffusing air pollutants and UHII during days of consistent winds (Alonso et al., 2007; Yang et al., 2021). Also, wind direction (WD) influence by WS has been reported to be a key factor in the variation of  $PM_{2.5}$  (Chen et al., 2020). The second component of the UMI is traditionally known as urban dryness island (UDI) intensity UDII, which is a phenomenon that compares the relative humidity (RH) of an urban area with that of the suburban/rural areas (Ackerman et al., 1978; Yang et al., 2017). RH is one of the popular measures that has been reported by several studies to be usually lesser than that of the suburban/rural areas in cities like London (England), Szeged (Hungary), Belgrade (Serbia), and Beijing (China) (Lee, 1991; Liu et al., 2009; Unger, 1999; Unkašević et al., 2001; Yang et al., 2017). For instance, in Shanghai, it was determined that the UHI phenomenon invariably coexists with UDIs (Zhou, 1994). Li et al. (2017b) also reported that an increase in RH could favor the hygroscopic growth of aerosols and enhance the formation of secondary aerosols, with the aqueous-phase reaction of  $SO_2$  and  $NO_2$  in fog/clouds or aerosol water leading to the formation of sulfate under hazy conditions in China. Although RH and UDII are significant components of urban-induced climatic effects, existing research on how UDII interacts with UHII and UPII is still insufficient.

Moreover, urban planetary boundary layer height (UPBLH) intensity (UPBLHI) is coined in this study to account for the difference in planetary boundary layer height (PBLH) between urban and rural areas. The PBLH is a fundamental meteorological variable that affects several tropospheric processes, such as aerosol patterns of distribution, convective activity, and cloud/fog deposition, which are crucial to reducing air pollution. As a result, PBLH has been utilized at a crucial length scale in meteorological, climate, and air quality models to assess turbulence mixing, vertical diffusion, convective transport, and atmospheric pollutant deposition (Du et al., 2013; Konor et al., 2009; Seibert et al., 2002; Yang et al., 2021). The strongest interactions between aerosols and meteorological variables take place in the PBL and are inherently connected to air pollution because of the bulk of aerosols residing in the PBL (Yu et al., 2002; Li et al., 2017b). Insightfully, the modeling of the UHI impact in mesoscale meteorological models is regarded to be crucial for the successful simulation of the urban boundary layer (UBL), which results in the dispersion and transport of air pollutants, thereby drastically alters the thermodynamic parameters of the UBL. For example, it has been demonstrated that the spatiotemporal variability of the boundary layer over Paris, France, is linked to the intensity of the UHI. (Giannaros et al., 2013; Quimbayo-duarte and Quimbayo-duarte, 2019). Therefore, since PBLH is a crucial component that is stabilized by aerosols, there is a need to investigate deeply the mechanisms and drivers for a better understanding of the interplay that existed between UHII and UPII in the cold region (especially Harbin) during the PHH periods.

Harbin, a city in the Northeastern part of China, has a prolonged winter season lasting for more than five months, which makes it unique from any other city in China. The average lowest temperature during

this season was approximately  $-37.7^{\circ}\text{C}$  (Yabo et al., 2023), resulting in extensive energy use (such as the burning of coal and biofuels) as heating systems, which inadvertently worsened the air quality of the city (Cheng et al., 2022). Until recently, little was known about the atmospheric chemistry in the cold environment of Harbin, including how it contributes to winter haze episodes in addition to other factors such as seasonal variations in weather and main emissions. Further insight was provided by Cheng et al. (2022) on the synergy of multiple drivers leading to severe winter haze pollution in Harbin. This lack of deep insight into the prevalent problem has hindered significant progress in air quality in Harbin compared to other cities (Chen et al., 2020; Xiao et al., 2021). In this study, the city of Harbin and its surrounding satellite towns were simulated during the early-winter-heavy-haze-episode (EWHHE; December 2019) and peak-winter-persistent-heavy-haze-episode (PWPHE; January 2020) in the heating period. The uniqueness of this period was that it covered the most polluted months encountered in recent years, which ranked Harbin among the top ten most polluted cities in China, with  $\text{PM}_{2.5}$  level concentration ranging from 150 to  $250\text{ }\mu\text{g}/\text{m}^3$ . This high value has not been seen between 2015 and 2020, according to air quality data from the China National Environmental Monitoring Center (CNEMC; <http://106.37.208.233:20035/>). The possible cause of this severe winter haze in Harbin was not based on anthropogenic emissions alone but rather on stable meteorological conditions (Zheng et al., 2015; Cheng et al., 2022). Based on the emission reduction policies over the years, anthropogenic emission inventory has contributed minimally, while changes in meteorological variables tend to influence air pollutants distribution and concentrations similar to the North China Plain (Wang et al., 2019). Moreover, the radiative mechanisms provide significant insight into how ARE increases the variation of aerosol loads and characteristics between urban and rural locations and tends to directly or indirectly impact UHII. Based on these underlying facts, this study probed into the radiative mechanisms and novel drivers' phenomena demonstrated in the form of USII, UDII, and UPBLHI, with WD which exerts significant influence on UHII andUPII during PHH, under various pollution levels using a regional numerical model referred to as the Weather Research and Forecasting model coupled with Chemistry (WRF-Chem). The model has been proven to be effective and efficient in simulating meteorological variables, air pollutants, and aerosol radiative effects (Fu et al., 2023; Skamarock et al., 2008; Yabo et al., 2023). In this study, the objectives were as follows: (1) investigate the radiative mechanisms influencing the spatial distribution of pollutant concentration on UHI and UPI; (2) examine the mechanisms and identify the drivers impacting UHI and UPI at different pollution levels in the cold region. Therefore, this study has provided insight into the radiative mechanisms and drivers that influence the coexistence of UHI and UPI in the cold region, hence contributing to urban climate and air pollution studies.

This paper mainly contains three parts; (1) location of the study, data used, configuration of the model, experimental design of the mechanisms, indices of estimating the drivers, and the evaluation matrices organized in Section 2. (2) The results and discussion are elaborated in Section 3. (3) The main conclusions are summarized in Section 4.

## 2. Materials and methods

### 2.1. Study area

Harbin is located in the Northeastern part of China, and it is the Heilongjiang provincial capital situated between latitude  $44^{\circ} 00'$  and  $46^{\circ} 24'$  N and longitude  $125^{\circ} 24'$  and  $130^{\circ} 06'$  E. It occupies a land area of about  $10,200\text{ km}^2$  and a population of slightly above five million people and is the third provincial capital in China (Chen et al., 2018b). A typical valley landform with an average height of 136 m can be used to describe the topography of the region. The northern area of Harbin is traversed by the XiaoXing'an Mountains, while the southern portion is bisected by the Zhangguangcai Ridge. Harbin's urban area is primarily

distributed along the three-ladder formation of the Songhua River, which passes through the city's center. Harbin is a very cold megacity with a minimum average air temperature of  $-37.7^{\circ}\text{C}$  and experiences strong anthropogenic activity more often in the city center than in the suburbs or the countryside, which impacts the air quality (Sun et al., 2020). During the winter season, the China Air Quality Monitoring (CAQM) platform reported that air pollution concentration has witnessed a significant decline annually from 2013 to 2018 (CAQM, 2022). Despite this decline, a slight hike in air pollution was observed prior to the COVID-19 outbreak (from mid-December 2019) and during the early stage of the outbreak in late January 2020 (peak in winter heavy-haze), showing a persistent rise in air pollution. It was on this note the period December 2019 to January 2020 was chosen to probe into the radiative mechanisms and drivers impacting UPI and UHI in the cold region.

## 2.2. Data

### 2.2.1. New static geographical land cover dataset

In this study, we used an up-to-date land cover dataset known as the Tsinghua University (represented as TU\_LC; Fig. 1b). With the TU\_LC, the urban-built-up land experienced noticeable changes describing these changes to be five times greater than those found in the USGS's standard land cover dataset (here referred to as USGS LC) (Fu et al., 2021b). More details on this new dataset have been described in our previous studies (Fu et al., 2021b; Yabo et al., 2022). Harbin city's land cover has substantially metamorphosed (Fig. 1(b)), resulting in impermeable surfaces, which has enhanced the impact of UHI (Yabo et al., 2022). The novel datasets included in this work have a significant influence on simulating meteorological variables, which are stimulated by the changes in the land surface and, subsequently, the pollutants. The purple and black ring roads represent the sub-urban and urban core, respectively. The different land use/cover types are shown in the legend of Fig. 1 (b).

### 2.2.2. Air pollution and meteorological data

The Multi-resolution Emission Inventory for China (MEIC) utilized in this study was last updated in 2017 at the time of this simulation (<http://www.meicmodel.org/dataset-meic.html>) and used to determine the sources of anthropogenic emissions of  $\text{PM}_{2.5}$ ,  $\text{PM}_{10}$ ,  $\text{SO}_2$ ,  $\text{NO}_2$ ,  $\text{CO}$ , and  $\text{O}_3$ , which were considered in this study from various sectors (residential, industry, power, and transportation). The MEIC being a major driver of the WRF-Chem model usually managed and updated by Tsinghua University was not up-to-date at the time of this simulation, which definitely contributed to the uncertainties during the simulation (Chen et al., 2020; Wang et al., 2019). In addition to the MIEC, another driver is the Model of Emissions of Gases and Aerosols from Nature (MEGAN) inventory, which was used to determine the sources of biogenic emissions based on weather and land use data. (Guenther et al., 2012). The MEGAN inventory was used as a default biogenic emissions data to run the WRF-Chem but has little effect during the winter due to the influence of snow cover and extreme cold on vegetation type and plant emission factors (Morichetti et al., 2022). In view of these concerns raised above, other studies adopted a similar approach despite the outdated MEIC and MEGAN datasets to have reasonable outcomes in the winter (Z. Chen et al., 2018a; Fu et al., 2021a; Li et al., 2023). Therefore, our study adopted a similar approach by considering December 2019 (here referred to as EWHHE) and January 2020 (PWPHE), with the inclusion of the radiative mechanisms. Hence, since residential sources accounted for the majority of the inventory, it must be updated. The observed data concentrations of  $\text{PM}_{2.5}$ ,  $\text{PM}_{10}$ ,  $\text{SO}_2$ ,  $\text{NO}_2$ ,  $\text{CO}$ , and  $\text{O}_3$  were downloaded from the China National Environmental Monitoring Center (<http://106.37.208.233:20035/>) to validate the simulated results.

The meteorological measurement data were sourced from the China Meteorological Data Service Centre (<http://data.cma.cn>) and were used to validate  $T_2$ , RH, WS, and WD. In Fig. 1 (b), the black triangles denote

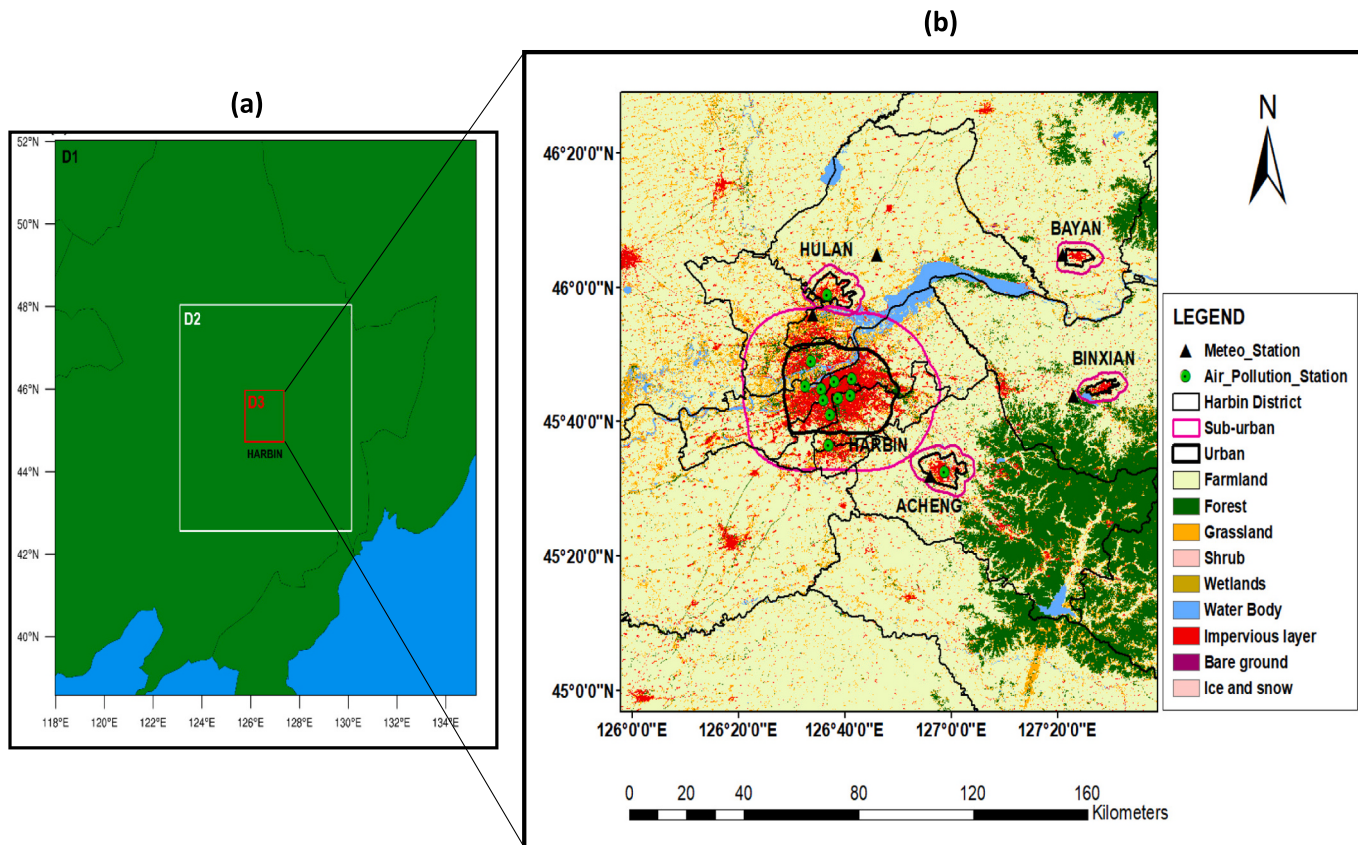


**Fig. 1.** (a) Domains in this study with horizontal spatial resolutions of 27 km (outermost domain) (D1), 9 km (D2; inner domain), and the focused innermost domain 3 km (D3) and (b) Shows the Tsinghua University land cover (TU\_LC) displayed in the innermost domain (Harbin) with a resolution of 1 km.

the meteorological stations, while the green dots represent the air pollution stations. The National Centers for Environmental Prediction (NCEP) final analysis data were used to extract the initial meteorological and boundary conditions with a horizontal precision of  $1^\circ \times 1^\circ$ . These initial and boundary conditions are major drivers that influence the meteorological variables, which have also been reported to contribute to the influence of air pollutants during the winter season (Fu et al., 2021a; Li et al., 2023). Therefore, uncertainties in meteorological fields could influence the modeling of aerosol transport and aerosol processes in the atmosphere (Wang et al., 2019).

### 2.3. Numerical modeling configuration

The WRF-Chem model (version 3.9.1.1) (Fast et al., 2006; Grell et al., 2005b; Skamarock et al., 2008) was applied to probe into the radiative mechanisms and drivers influencing UHI and UPI during heavy-haze events in Harbin, Northeast China. The model has been proven to be effective and efficient in simulating meteorological variables, air pollutants, and aerosol radiative effects (Fu et al., 2023; Grell et al., 2005a; José et al., 2013; Skamarock et al., 2008; Yabo et al., 2023). Based on these facts, it was capable of probing the radiative mechanisms and drivers impacting UPI and UHI. The WRF-Chem simulations were done on triple nested domains, which is in agreement with our previous studies (Fu et al., 2021a; Yabo et al., 2023). The triple nested domain resolutions were as follows: 27 km  $\times$  27 km, 9 km  $\times$  9 km, and 3 km  $\times$  3 km (Fig. 1 (a)). The innermost domain covered downtown Harbin and its environs (Fig. 1 (b)). The most popular schemes used in the Northern part of China, according to prior studies, are displayed in Table 1. In order to operate WRF-Chem and simulate air contaminants, the meteorological conditions produced by WRF were employed. The simulations were conducted in December 2019 (EWHHE) and January 2020

**Table 1**  
Model configuration.

| Model configuration name         | Parameters   |
|----------------------------------|--|
| Domain size                      | 55 $\times$ 55, 67 $\times$ 67, 46 $\times$ 46                     |
| Horizontal resolution            | 27 km $\times$ 27 km, 9 km $\times$ 9 km, 3 km $\times$ 3 km       |
| Vertical Level                   | 30 vertical levels   |
| Spin-up                          | 48-h   |
| Modeling episode                 | December 2019 (EWHHE), January 2020 (PWPHE)                        |
| Microphysics                     | Purdue Lin microphysics scheme (Lin et al., 1983)                  |
| Land surface scheme              | Noah's land surface model (Chen and Dudhia, 2001)                  |
| Surface layer                    | Revised MM5 Monin-Obukhov scheme                                   |
| Planetary boundary layer scheme  | YSU (Hong et al., 2006)  |
| Longwave radiation scheme        | RRTM (Mlawer et al., 1997)   |
| Shortwave radiation scheme       | NOAA Goddard (Chou et al., 2001)                                   |
| Cumulus schemes                  | Grell-Devenyi (Grell and Dévényi, 2002; Grell et al., 2005b)       |
| Boundary and initial conditions  | NCEP-FNL $1^\circ \times 1^\circ$ reanalysis data                  |
| Gas-phase chemistry scheme       | RADM2 (Stockwell et al., 1997)                                     |
| Photolysis scheme                | Fast-J scheme (Wild et al., 2000)                                  |
| Aerosol scheme                   | MADE, SORGAM (Ackermann et al., 1998; Schell et al., 2001)         |
| Anthropogenic emission inventory | MEIC ( <a href="http://meicmodel.org/">http://meicmodel.org/</a> ) |
| Biogenic emission inventory      | MEGAN (Guenther et al., 2012)                                      |

(PWPHE), with the initial two days being discarded (called “spin-up”).

### 2.4. Experimental design of radiative mechanisms

In this study, we selected December 2019 (EWHHE) and January

2020 (PWPHE) based on the measurement data obtained from the China National Environmental Monitoring Center, which revealed an unusual rise in air pollution after experiencing a progressive decline in the winter of January 2017 to December 2018 (Fig. 2). The winter span through January 2019, depicted a rise in PM<sub>2.5</sub> and air quality (AQI) with monthly average values of 90.93 µg/m<sup>3</sup> and 123.12 µg/m<sup>3</sup> (Fig. 2; shown in magenta-dotted rectangular line) compared with the January 2018 (PM<sub>2.5</sub>: 73.51 µg/m<sup>3</sup> and AQI: 99.28 µg/m<sup>3</sup>), which are above the China air quality standard value of 50 µg/m<sup>3</sup>. This persistent rise in air pollution was experienced from late December 2019 (with monthly average AQI value of 99.00 µg/m<sup>3</sup> and PM<sub>2.5</sub> of 91.00 µg/m<sup>3</sup>) through January 2020 (with monthly average AQI value of 227.00 µg/m<sup>3</sup> and PM<sub>2.5</sub> of 104.23 µg/m<sup>3</sup>) known as the peak of the heavy-haze event coinciding with the early lockdown of the COVID-19 pandemic (Fig. 2; shown in red-dotted rectangular line). It is on this note that this study tried to probe into the radiative mechanisms and the drivers influencing the changes in UHI and UPI. From Table 2, we designed four mechanisms during the simulation, which are as follows: non-radiative effect (NRE), direct radiative effect (DRE), indirect radiative effect (IRE), and slope-and-shading effect (SSE). The first is the NRE, which is a default setting with the other mechanisms being inactive except the default shortwave radiation included in the simulation. Secondly, the DRE was activated by tuning the shortwave radiation alongside the chemistry. Thirdly, the DRE and the aqueous phase chemistry variables were adjusted to activate the IRE. Lastly, the SSE is a combined radiative effect whereby the IRE is combined together with the SSE, which is topography dependent. The default parameters of the SSE when considered in the model tend to capture the topographic of the region, being a typical valley landform with Mountains on the northern and southern parts of the city. This study was not designed to holistically

**Table 2**  
Mechanisms and simulation design.

| S/<br>N | Mechanisms | New land cover<br>dataset/<br>Anthropogenic<br>emissions | Direct-<br>radiative-<br>effect | Indirect-<br>radiative-<br>effect | Slope-<br>and-<br>shading-<br>effect |
|---------|------------|--|---------------------------------|-----------------------------------|--------------------------------------|
| 1       | NRE        | TU_LC; MEIC  | in-active                       | in-active                         | in-active                            |
| 2       | DRE        | TU_LC; MEIC  | active                          | in-active                         | in-active                            |
| 3       | IRE        | TU_LC; MEIC  | active                          | active                            | in-active                            |
| 4       | SSE        | TU_LC; MEIC  | active                          | active                            | active                               |

NRE represents the non-radiative effect; DRE represents the direct-radiative-effect; IRE is known as the indirect-radiative-effect, a combined effect DRE + IRE; SSE represents the slope-and-shading effect, a combined effect IRE+SSE. Tsinghua University land cover is represented as TU\_LC, while the Multi-resolution Emission Inventory for China is represented as MEIC.

examine the impact of topography on meteorological variables and air pollution but was limited to some radiative mechanisms. The updated anthropogenic emissions and the new geographical dataset used were MEIC (2017) and Tsinghua land cover (TU\_LC), respectively. Therefore, different radiative mechanisms were adopted in order to probe the meteorological drivers that influence the changes in the UHI and the UPI.

## 2.5. Indices and methods of estimating drivers (urban meteorology islands) and urban pollution islands

The various drivers that are components of the urban meteorology islands (UMI) estimated were as follows: (1) UHII/UCII, (2) USII, (3) UDII, and (4) UPBLHI. On the other hand, the index of the UPI was estimated alongside the categorization of pollution levels of different air

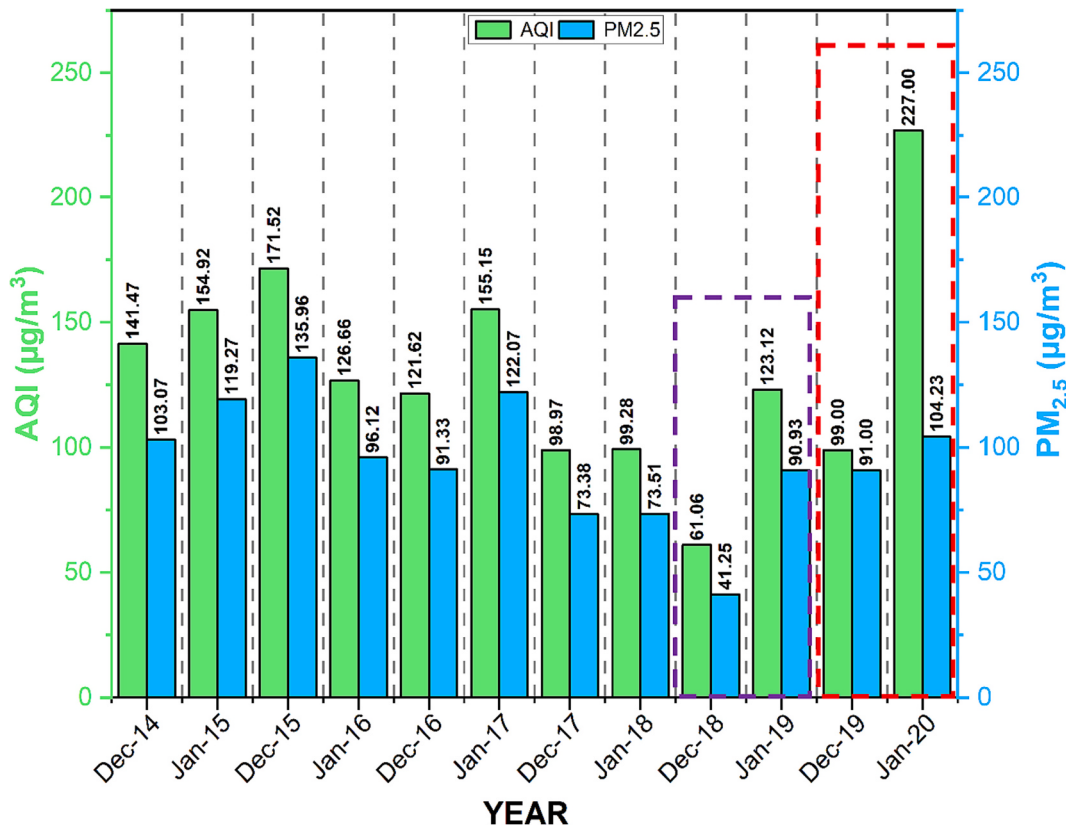


**Fig. 2.** Selection of the periods of simulation based on the air quality (AQI) and PM<sub>2.5</sub> of winter of December 2014 and January 2015 to December 2019 (early winter heavy-haze episode; EWHHE) and January 2020 (peak winter persistent-heavy-haze episode; PWPHE). The magenta-dotted rectangular line represents December 2018 (shows a decline in air pollution) and January 2019 (slight increase in air pollution). The red-dotted rectangular line represents the periods considered in this study. (For interpretation of the references to colour in this figure legend, the reader is referred to the web version of this article.)

pollutants.

### 2.5.1. Calculating urban heat/cold island intensity (UHII/UCII)

In quantifying UHI, multiple indices that are based on either surface or air temperatures are used. In this study, we used an air-based UHI index (the UHII), which measures the average temperature variance between the ambient air temperature in a particular metropolitan area and that of a sample suburban or rural location. It is crucial to choose the right location to represent the suburbs and rural regions because a poor choice could lead to inaccurate estimations of UHI and its effects. (Runnalls and Oke, 2000). To minimize inaccurate estimations of UHI linked to the inadequate choice of typical rural areas, the World Meteorological Agency (WMA) suggests criteria for the right selection of representative urban areas (Oke, 2006), which was used in this study. For instance, it is advisable to include typical rural areas on flat vegetated land. Runnalls and Oke (2000) reported that there are tendencies where UHI could be positive ( $T_{urban} > T_{rural}$ ), negative ( $T_{rural} > T_{urban}$ ), and neutral ( $T_{urban} = T_{rural}$ ). In this study, we experienced situations whereby the  $T_{urban} > T_{rural}$ , which we considered as UHII (eq. 1), while  $T_{rural} > T_{urban}$  and we called “urban cold island” (UCI) intensity (UCII) expressed in eq. (2).

$$UHII = T_{urban} - T_{sub-urban/rural} \quad (T_{urban} > T_{rural}) \quad (1)$$

$$UCII = T_{urban} - T_{sub-urban/rural} \quad (T_{rural} > T_{urban}) \quad (2)$$

where UHII and UCII are the urban heat island intensity and urban cold island intensity ( $^{\circ}\text{C}$ ), respectively.  $T_{urban}$  and  $T_{sub-urban/rural}$  are the  $T_2$  ( $^{\circ}\text{C}$ ) of an urban and suburban/rural areas counterpart, respectively.

### 2.5.2. Calculating urban stilling island intensity (USII)

Wind speed (WS) is one of the meteorological drivers of both UHII and UPII, and it is an important indicator in urban climatology, which is also known as wind stilling (Hou et al., 2013). It is imperative to note that the accumulation and storage of air pollutants and heat are favored by low WS, while high WS helps in diffusing air pollutants and UHII during days of consistent winds (Alonso et al., 2007; Yang et al., 2021). Therefore, the variance in WS between the urban and suburban/rural areas is known as the urban stilling island (USII) intensity (Yang et al., 2020a, 2020b). The WS at 10 m was used at the urban station, denoted as  $WS_{urban}$ , while the suburban/rural station WS is also denoted as  $WS_{sub-urban/rural}$ . Yang et al. (2020a, 2020b) obtained an expression for USII, which was slightly modified in this study in order to achieve the desired objective. The USII is expressed in eq. (3) as:

$$USII = \Delta WS_{sub-urban/rural-urban} = -(WS_{urban} - WS_{sub-urban/rural}) \quad (3)$$

### 2.5.3. Calculating urban dryness island intensity (UDII)

The second meteorological driver considered in this study was the relative humidity (RH), which is a significant climatic variable uniquely different in urban areas with respect to its sub-urban/rural area counterparts. Several studies have found that RH in cities is usually lesser than that in suburban/rural areas (Lee, 1991; Liu et al., 2009; Unger, 1999; Unkašević et al., 2001; Yang et al., 2017), which is a phenomenon traditionally known as urban dryness island (UDII) and the intensity is measured as UDII (Ackerman et al., 1978; Yang et al., 2017). In this study, the UDII was calculated by comparing the RH in urban and sub-urban/rural areas. The urban RH ( $RH_{urban}$ ) is the average value of any urban station (here referred to as downtown Harbin), while the suburban/rural ( $RH_{suburban/rural}$ ) is the average value of RH in the suburban/rural station (here referred to as Acheng satellite town). Therefore, UDII is expressed in eq. (4) as;

$$UDII = \Delta RH_{suburban/rural-urban} = -(RH_{urban} - RH_{suburban/rural}) \quad (4)$$

### 2.5.4. Calculating urban planetary boundary layer height intensity (UPBLHI)

The PBLH is a fundamental variable that affects several tropospheric processes, including aerosol patterns of distributions, convection activity, and cloud/fog formation, that are crucial to reducing air pollution. As a result, PBLH has been utilized at a crucial length scale in meteorological, climate, and air quality models to assess turbulence mixing, vertical diffusion, convective transport, and atmospheric pollutant deposition (Du et al., 2013; Konor et al., 2009; Seibert et al., 2002; Yang et al., 2021). In this study, we tried to introduce also a phenomenon which is known as urban planetary boundary layer height intensity (UPBLHI) to depict the difference between the urban boundary layer (represented as  $PBLH_{urban}$ ) and the suburban/rural boundary layer (represented as  $PBLH_{suburban/rural}$ ). The UPBLH phenomenon is expressed in eq. (5) as follows;

$$UPBLH = \Delta PBLH_{urban-suburban/rural} = (PBLH_{urban} - PBLH_{suburban/rural}) \quad (5)$$

### 2.5.5. Calculating Urban Pollution Island Intensity (UPII)

In the same vein, a phenomenon known as the urban pollution island (UPI) intensity (UPII) was recently coined by some studies (Li et al., 2018; H. Li et al., 2020), although it has been in existence since in the 1990s (Shuzhen et al., 1991) and has been known as the urban turbidity island (UTI) intensity (UTII). The UPII/UTII is the difference in air pollutants between the urban and the suburban/rural areas, which are defined in a similar form as the UHII. To compute the UPII, we found the average of each air pollutant ( $\text{PM}_{2.5}$ ,  $\text{PM}_{10}$ ,  $\text{SO}_2$ ,  $\text{NO}_2$ , CO, and  $\text{O}_3$ ) in the urban environmental stations within the inner ring road and the satellite town (suburban/rural) environmental stations (For example,  $\text{PM}_{urban}$  for urban area and  $\text{PM}_{suburban/rural}$ . The  $\text{PM}_{(2.5/10)}$  is used to derive eq. (6), which was applied to other air pollutants such as  $\text{SO}_2$ ,  $\text{NO}_2$ , CO, and  $\text{O}_3$  (See Table S3, S4, S5, and S6 for outcome).

$$UPII = PM_{urban} - PM_{suburban/rural} \quad (6)$$

where UPII is urban pollution island intensity ( $\mu\text{g}/\text{m}^3$ ),  $PM_{urban}$  and  $PM_{suburban/rural}$  are the particulate matter (2.5/10 diameter) of the urban setting ( $\mu\text{g}/\text{m}^3$ ) and the suburban/rural area counterparts, respectively.

### 2.5.6. Categorization of pollution levels of different air pollutants

In this study, we considered the different air pollutant levels according to China's national air quality standard and then divided the UHII, UPII, and other meteorological drivers based on six different pollutant levels (Yang et al., 2021). The details of this categorization of different pollutant levels are shown in the supplementary material Table S1.

### 2.6. Model evaluation metrics

In this study, the simulated results from the model were evaluated using the following statistical evaluation metrics: mean bias (MB), mean absolute error (MAE), normalized mean error (NME), root mean square error (RMSE), and the Pearson correlation coefficient (R). These aforementioned metrics were used because it has been shown that they are appropriate markers for determining variance and inconsistencies between the simulated and observed data (Fu et al., 2021a, 2023; Li et al., 2023; Yabo et al., 2022, 2023). The equations (Eq. 7–11) below were used for the evaluation of our simulated results.

$$MB = \frac{1}{n} \sum_{i=1}^n (T_{s,i} - T_{o,i}) \quad (7)$$

$$MAE = \frac{1}{n} \sum_{i=1}^n |(T_{s,i} - T_{o,i})| \quad (8)$$

$$NME = \frac{1}{n} \sum_{i=1}^n |(\text{sim}_i - \text{obs}_i)| / \text{obs}_i \quad (9)$$

$$\text{RMSE} = \sqrt{\frac{\sum_{i=1}^n (T_{s,i} - T_{o,i})^2}{n}} \quad (10)$$

$$\text{Corr}(R) = \frac{1}{n-1} \sum_{i=1}^n \left( \frac{T_{s,i} - \mu_{T_s}}{\sigma_{T_s}} \right) \left( \frac{T_{o,i} - \mu_{T_o}}{\sigma_{T_o}} \right) \quad (11)$$

Where  $T_{o,i}$ ,  $T_{s,i}$  represent the observed and simulated temperatures at the time  $i$  and grid  $i$  for  $T_2$  ( $^{\circ}\text{C}$ ), respectively. The mean temperatures and standard deviation are represented as  $\mu$  and  $\sigma$ , respectively. The frequency of the data is denoted as  $n$ . The  $sim_i$  and  $obs_i$  represents the simulated and observed results.

The NCAR Command Language (NCL) software was used to extract the meteorological variables and air pollutants data within the innermost domain (D3) at grid points and within the buffers, delineating the core of the downtown and their corresponding suburbs (NCL, 2019). The NCL has been widely used for the extraction of spatial and time series datasets (Fu et al., 2021a, 2023; Li et al., 2023). The Origin Pro (version 2021) was used for plotting most of the linear charts displayed in this study.

### 3. Results and discussion

#### 3.1. Validation of model-simulated results

The simulated results for the meteorological variables and air pollutants concentrations were verified with respect to their corresponding hourly observation data in this section for the periods of EWHHE and PWPHHE.

##### 3.1.1. Evaluation of meteorological variables

Since meteorological variables play a significant role in influencing the distribution of aerosols, this study first evaluates the model-simulated results in comparison with the hourly observation data (Fig. 3). We adopted two meteorological stations (one representing the urban area (Harbin) and the other the satellite town (Acheng)) to evaluate the outcome from the model-simulated results. In this study, the simulated meteorological variables agree well with the observations from the average of the four mechanisms (NRE, DRE, IRE, and SSE) evaluated (as shown in Fig. 3 (a) – (h)), but the average values were used in our presentation (Table S2). The statistical parameters adopted for the evaluation in comparison between the model-simulated meteorological variables and the corresponding observation data were MB, MAE, NME, and RMSE. During the EWHHE, the average values of  $T_2$  (shown in Fig. 3 (a) and Table S2) for MB and MAE were  $1.96\ ^{\circ}\text{C}$  and  $2.46\ ^{\circ}\text{C}$ , respectively. Likewise, the NME and RMSE accounted for  $0.17$  and  $3.01\ ^{\circ}\text{C}$ ,

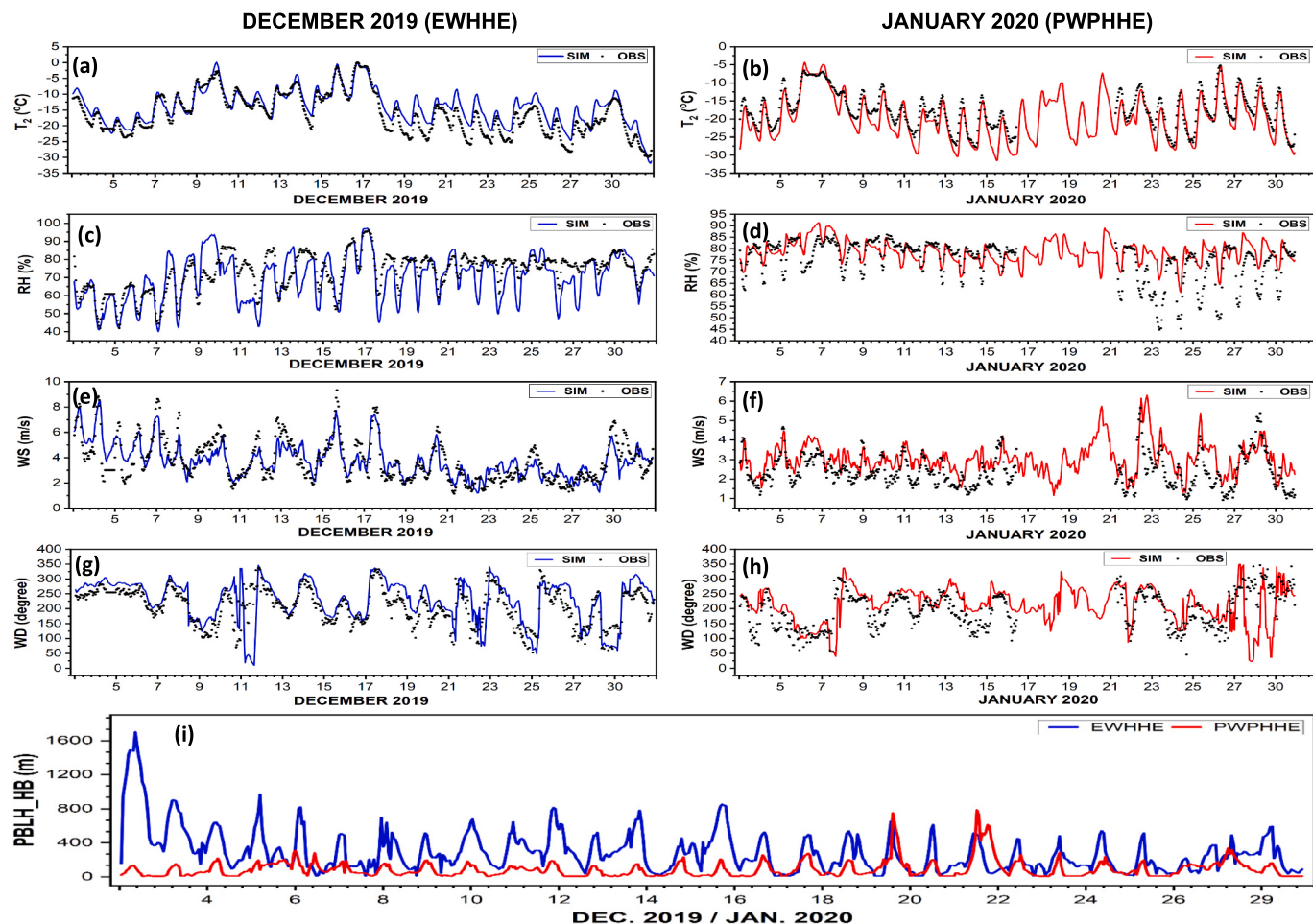


**Fig. 3.** Average hourly time series of  $T_2$ , RH, WS, and WD in December 2019 (EWHHE; (a), (c), (e), and (g)) and January 2020 (PWPHHE; (b), (d), (f), and (h)). The PBLH for the EWHHE and PWPHHE are shown in (i). The black dots in all the figures represent the observations, while the solid blue and red lines represent the simulations of EWHHE and PWPHHE, respectively. Note: EWHHE and PWPHHE represent the early winter heavy-haze episode and peak winter heavy-haze episode, respectively. PBLH\_HB represent the PBLH of Harbin (HB). (For interpretation of the references to colour in this figure legend, the reader is referred to the web version of this article.)

respectively. The average R-value for the  $T_2$  accounted for 0.94, revealing a very high correlation between the simulated and the observed with minimal bias. For the RH (Fig. 3 (c) and Table S2), the model-simulated results were in agreement with the observation, having average values of  $-3.83\%$ ,  $7.47\%$ ,  $0.10$ , and  $9.76\%$  corresponding to MB, MAE, NME, and RMSE, respectively. The average R-value derived from NRE, DRE, IRE, and SSE was 0.71 during the EWHHE. Similarly, the average values of WS and WD (Fig. 3 (e) and (g); Table S2) account for MB ( $0.02 \text{ m/s}$  and  $21.85^\circ$ ), MAE ( $0.77 \text{ m/s}$  and  $41.32^\circ$ ), NME ( $0.23$  and  $0.24$ ), RMSE ( $0.95 \text{ m/s}$  and  $57.51^\circ$ ), and R ( $0.82$  and  $0.67$ ). It was observed from the evaluation of all the meteorological variables during the EWHHE, that  $T_2$  has the highest R-value followed by WS, RH, and WD, hence, revealing the strength of their relationship between the simulated and observation data, which was also in agreement with other studies (M. Li et al., 2017b; Wang et al., 2019). The minimum value of deviations from MB, MAE, and RMSE recorded in WS, possibly could be as a result of the low wind speed, while that for NME was observed in RH during the EWHHE.

In considering the PWPHE, the average hourly  $T_2$  (Fig. 3 (b) and Table S2) values for the MB, MAE, NME, RMSE, and R were  $-5.21^\circ \text{C}$ ,  $5.57^\circ \text{C}$ ,  $0.14$ ,  $8.88^\circ \text{C}$ , and  $0.92$ , respectively. Likewise, for the RH (Fig. 3 (d) and Table S2), the average values of the evaluation results were as follows: MB ( $16.91\%$ ), MAE ( $18.75\%$ ), NME ( $0.07$ ), RMSE ( $34.06\%$ ), and R ( $0.59$ ). Typically, the diurnal pattern for  $T_2$  and RH (Fig. 3 (a)-(d)) between the simulated and the observed data matches well in most cases and was slightly overestimated and underestimated in some cases (in both EWHHE and PWPHE). We discovered that  $T_2$  and RH during the PWPHE performed relatively poorly compared with the EWHHE, possibly because of the uncertainties originating from the meteorological fields (initial and boundary conditions), which are major drivers that could have influenced our simulations. RH simulation has been reported to be sensitive to surface temperature (Bei et al., 2017), which also exerts influence on air temperature. The outcomes from this study are in agreement with previous studies (M. Li et al., 2017b; Wang et al., 2019; Fu et al., 2023). Similarly, the mean errors for WS and WD observed during the PWPHE were MB ( $1.03 \text{ m/s}$  and  $53.16^\circ$ ), MAE ( $1.18 \text{ m/s}$  and  $80.92^\circ$ ), NME ( $0.32$  and  $0.25$ ), and RMSE ( $1.61 \text{ m/s}$  and  $113.95^\circ$ ), while the R values accounted for  $0.57$  and  $0.39$ , respectively. The simulated WS results were generally consistent with the observation. The MB and the RMSE of the model-simulated WS agree with the standard criteria set by the European Environment Agency (European Environment Agency, 2011) as well as the study by Fu et al. (2023). Likewise, the WD showed the same pattern as the WS, indicating relatively good performance in both variables. The NMEs for the WS and WD during the EWHHE were slightly larger than during the PWPHE, revealing the dominant effect of the persistent heavy haze event with low wind speed. Moreover, the PBLH (Fig. 3 (i)) for both EWHHE and PWPHE revealed a good tendency with the PWPHE being lower than EWHHE due to the persistent heavy haze, which tends to lower the PBLH. Generally, it is worth noting that the WRF-Chem model accurately captured the time variation and magnitude of  $T_2$ , RH, WS, and WD with only about  $<5\%$  of the observation data missing during the PWPHE. For instance, comparing the PWPHE and EWHHE, the simulated  $T_2$ , WS, WD, and PBLH were decreased by  $5.46^\circ \text{C}$ ,  $0.78 \text{ m/s}$ ,  $15.67^\circ$ , and  $208.75 \text{ m}$ , respectively, with an accompanying  $9.10\%$  increase in RH (Table S2). Typically, on average from the radiative mechanisms, the PWPHE is characterized by low  $T_2$ , WS, and PBLH with high RH. The matrices used are in agreement with other studies (Tao et al., 2018; Fu et al., 2023; B. Li et al., 2020). Although the model is generally good at simulating air pollutants, radiative mechanisms, and meteorological drivers, the uncertainties from emission inventory and meteorological fields still have the potential to impact ARE evaluation (Wu et al., 2019).

### 3.1.2. Evaluation of the incorporated updated geographical datasets based on meteorological variables

In order to have detailed surface features captured in our simulation, this study evaluated the responses of meteorological variables ( $T_2$ , RH, WS, and WD) with respect to the changes in the new land cover dataset (TU\_LC) compared with the default dataset (USGS). Fig. S1 ((a), (b), (c), (d)) shows the meteorological variables of the new land cover dataset were all in agreement with the meteorological variables of the default dataset. The TU\_LC and USGS\_LC have the same R values of  $0.94$  and  $0.71$  for  $T_2$  and RH, respectively, while WS and WD were  $0.82$  and  $0.63$  (for TU\_LC) and  $0.83$  and  $0.66$  (for USGS\_LC), respectively.

We further investigated the performance of these meteorological variables using Taylor's diagram (Fig. S1 (e), (f), and (g)). It was discovered that  $T_2$  has the best performance in the DRE, IRE, and SSE, with the strongest correlation and the lowest ratio of standardized deviation. This agrees with our previous studies on the performance of  $T_2$  with respect to the TU\_LC, MODIS\_LC, and USGS\_LC (Fu et al., 2021a, 2021b; Yabo et al., 2022) after the  $T_2$  is the WS  $>$  RH  $>$  WD. The study by Fu et al. (2021b) also confirmed the similar performance of these datasets with respect to the meteorological variables.

### 3.1.3. Evaluation of air quality-related pollutants

The model-simulated air pollutant concentrations were evaluated with the observation data derived from the website of the China National Environmental Monitoring Center (CNEMC, <http://113.108.142.147:20035/emcpublish/>). The simulated pollutants considered were PM<sub>2.5</sub>, PM<sub>10</sub>, SO<sub>2</sub>, NO<sub>2</sub>, CO, and O<sub>3</sub> within the downtown and the satellite town (Fig. 4, Table S3). As shown in Table S3, the statistical parameters used in evaluating the model performance include MB, MAE, NME, RMSE, and R for the EWHHE and PWPHE.

For the EWHHE (shown in Fig. 4 (a), (c), (e) (g), (i), and (k); Table S3), the simulated pollutants were observed to match the observation data, with a good performance. The simulated pollutants such as SO<sub>2</sub>, CO, and O<sub>3</sub>, were majorly overestimated, with PM<sub>2.5</sub>, PM<sub>10</sub>, and NO<sub>2</sub> slightly being underestimated during the EWHHE. The minimum error values of the MB, MAE, NME, and RMSE for the PM<sub>2.5</sub> were observed at  $-10.55 \mu\text{g/m}^3$  (NRE),  $41.07 \mu\text{g/m}^3$  (DRE),  $0.53$  (DRE),  $56.31 \mu\text{g/m}^3$  (DRE), respectively, while the high R-value was accounted for  $0.62$  (for both DRE and IRE). Likewise, a similar pattern was also observed for the PM<sub>10</sub> accounting for the minimum error values to be  $-1.87 \mu\text{g/m}^3$  (NRE),  $44.99 \mu\text{g/m}^3$  (DRE),  $0.47$  (NRE and DRE), and  $60.10 \mu\text{g/m}^3$  (DRE) for MB, MAE, NME, and RMSE, respectively. The R-value was observed at  $0.63$  for PM<sub>10</sub>, which was slightly higher than that of PM<sub>2.5</sub>. Besides, SO<sub>2</sub> and NO<sub>2</sub> had their minimum errors majorly at the NRE for MB ( $6.09 \mu\text{g/m}^3$  and  $87.93 \mu\text{g/m}^3$ ), MAE ( $11.80 \mu\text{g/m}^3$  and  $91.51 \mu\text{g/m}^3$ ), NME ( $0.37$  and  $1.00$ ), and RMSE ( $15.09 \mu\text{g/m}^3$  and  $112.51 \mu\text{g/m}^3$ ), respectively. It could be deduced from these errors that introducing the various aerosol radiative effects contributed slightly to the changes observed in the simulation, which also could be traced to the uncertainties in the emission inventory. The R-values for the SO<sub>2</sub> and NO<sub>2</sub> accounted for  $0.62$  (DRE) and  $0.60$  (SSE), respectively, which was in agreement with other findings (Wang et al., 2019). It was also observed during the EWHHE that CO and NO<sub>2</sub> had the largest biases compared to the other pollutants. The O<sub>3</sub> had the lowest NME at the IRE and SSE accounting for  $0.33$  with an R-value of  $0.51$ .

During the PWPHE (Fig. 4 (b), (d), (f), (j), and (l); Table S3), the simulated pollutants were in agreement and closely matched the observation data. The simulated pollutants, especially PM<sub>2.5</sub>, PM<sub>10</sub>, SO<sub>2</sub>, and CO were majorly underestimated having MB for NRE ( $-52.48 \mu\text{g/m}^3$ ,  $-35.98 \mu\text{g/m}^3$ ,  $-14.36 \mu\text{g/m}^3$ , and  $-432.77 \mu\text{g/m}^3$ ) and DRE ( $-69.09 \mu\text{g/m}^3$ ,  $-30.25 \mu\text{g/m}^3$ ,  $-12.81 \mu\text{g/m}^3$ , and  $-387.53 \mu\text{g/m}^3$ ), with NO<sub>2</sub> and O<sub>3</sub> slightly overestimated at NRE ( $63.36 \mu\text{g/m}^3$  and  $68.28 \mu\text{g/m}^3$ ) and ( $29.79 \mu\text{g/m}^3$  and  $30.25 \mu\text{g/m}^3$ ), respectively. Moreover, the IRE and SSE scenarios, the PM<sub>2.5</sub> ( $-12.82 \mu\text{g/m}^3$  and  $-12.73 \mu\text{g/m}^3$ ), SO<sub>2</sub> ( $-12.24 \mu\text{g/m}^3$  and  $-12.23 \mu\text{g/m}^3$ ), and CO ( $-392.55 \mu\text{g/m}^3$  and  $-392.38 \mu\text{g/m}^3$ ) were underestimated with PM<sub>10</sub> ( $12.98 \mu\text{g/m}^3$  and

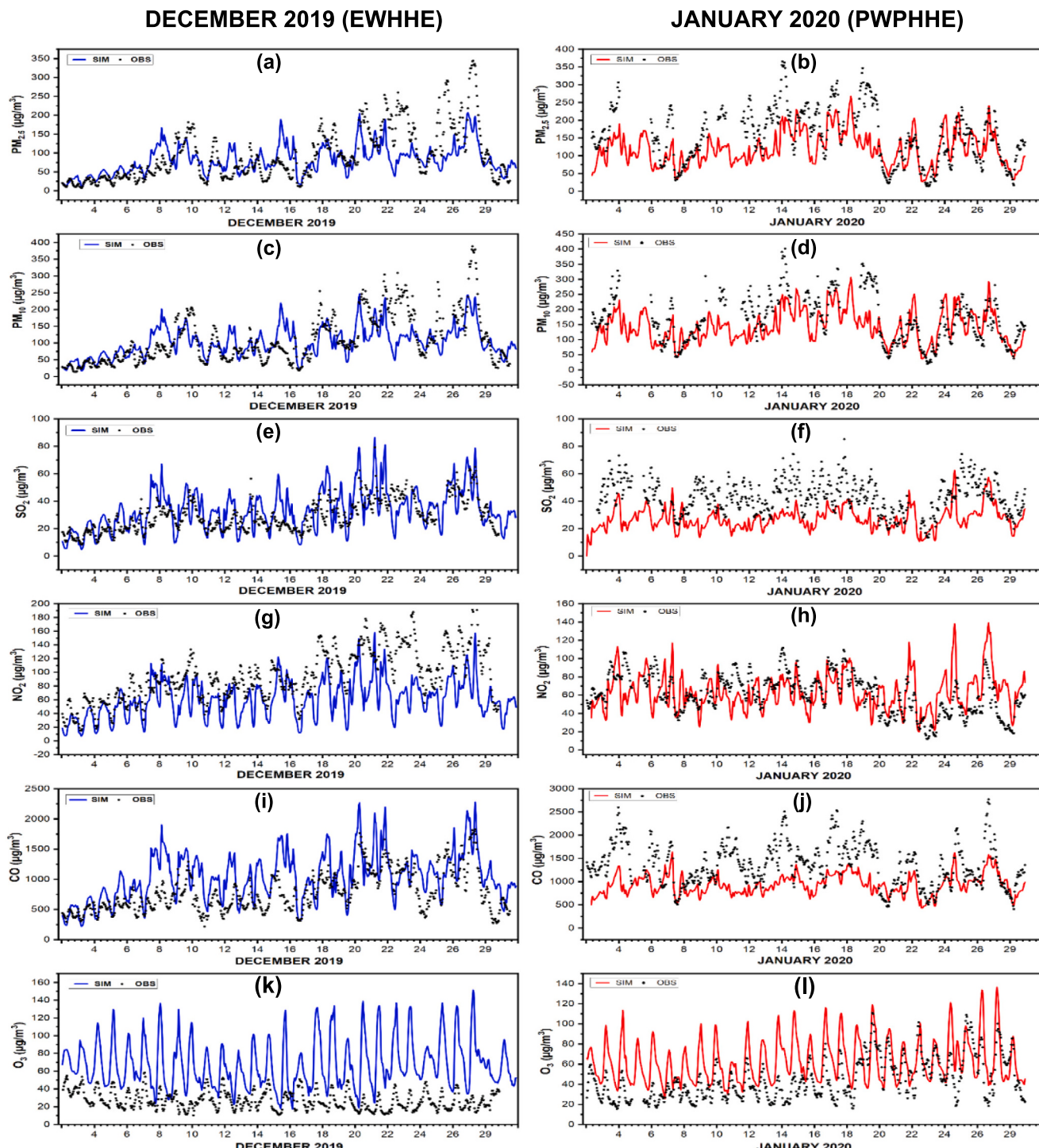


**Fig. 4.** Time series evaluation of air quality-related pollutants (PM<sub>2.5</sub>, PM<sub>10</sub>, SO<sub>2</sub>, NO<sub>2</sub>, CO, and O<sub>3</sub> ( $\mu\text{g}/\text{m}^3$ )) of simulated and observed. The black dots denote observed values, while the solid blue and red lines represent the simulated values for both December 2019 (EWHHE; (a), (c), (e), (g), (i), and (k)) and January 2020 (PWPHE; (b), (d), (f), (h), (j), and (l)), respectively. The simulated and observed concentrations are averaged over the downtown and the satellite town stations. Note: EWHHE and PWPHE represent the early winter heavy-haze episode and peak winter heavy-haze episode, respectively. (For interpretation of the references to colour in this figure legend, the reader is referred to the web version of this article.)

13.08  $\mu\text{g}/\text{m}^3$ , NO<sub>2</sub> (69.59  $\mu\text{g}/\text{m}^3$  and 69.61  $\mu\text{g}/\text{m}^3$ ), and O<sub>3</sub> (19.13  $\mu\text{g}/\text{m}^3$  and 19.14  $\mu\text{g}/\text{m}^3$ ) overestimated. The underestimation and reduction of air pollutants were attributed to related outcomes of the Chinese government policies of shutting down factories with high energy consumption and high pollution emissions (Li and Han, 2016; Wang et al., 2017; Zhang et al., 2020). The MB for all the pollutants were discovered to be lower in PWPHE than EWHHE except for O<sub>3</sub> showing the reverse

in all the scenarios such as NRE (29.79  $\mu\text{g}/\text{m}^3 > 13.26 \mu\text{g}/\text{m}^3$ ), DRE (30.25  $\mu\text{g}/\text{m}^3 > 13.22 \mu\text{g}/\text{m}^3$ ), IRE (19.13  $\mu\text{g}/\text{m}^3 > 2.87 \mu\text{g}/\text{m}^3$ ), and SSE (19.14  $\mu\text{g}/\text{m}^3 > 2.48 \mu\text{g}/\text{m}^3$ ). The MAE and RMSE for all the pollutants were lower in EWHHE than the PWPHE simulation except for NO<sub>2</sub>, showing the MAE and RMSE in EWHHE greater than the PWPHE simulation in all the mechanisms as follows: NRE (91.51  $\mu\text{g}/\text{m}^3 > 64.10 \mu\text{g}/\text{m}^3$  and 112.51  $\mu\text{g}/\text{m}^3 > 75.90 \mu\text{g}/\text{m}^3$ ), DRE (94.08  $\mu\text{g}/\text{m}^3 > 68.76 \mu\text{g}/\text{m}^3$  and 116.08  $\mu\text{g}/\text{m}^3 > 80.50 \mu\text{g}/\text{m}^3$ ), IRE (19.13  $\mu\text{g}/\text{m}^3 > 2.87 \mu\text{g}/\text{m}^3$ ), and SSE (19.14  $\mu\text{g}/\text{m}^3 > 2.48 \mu\text{g}/\text{m}^3$ ).

$\mu\text{g}/\text{m}^3$  and  $114.70 \mu\text{g}/\text{m}^3 > 79.69 \mu\text{g}/\text{m}^3$ ), IRE ( $96.01 \mu\text{g}/\text{m}^3 > 70.10 \mu\text{g}/\text{m}^3$  and  $117.08 \mu\text{g}/\text{m}^3 > 81.20 \mu\text{g}/\text{m}^3$ ), and SSE ( $107.95 \mu\text{g}/\text{m}^3 > 70.11 \mu\text{g}/\text{m}^3$  and  $131.27 \mu\text{g}/\text{m}^3 > 81.21 \mu\text{g}/\text{m}^3$ ). The NME values of 0.25 and 0.30 for  $\text{PM}_{10}$  (in IRE and SSE) and CO (in DRE) were observed in PWPHHE, respectively. These were found to be within the stipulated criteria limits of  $\text{NME} \leq 30\%$  (Boylan and Russell, 2006; Li et al., 2023), revealing the model performance to be good. The R values for  $\text{PM}_{2.5}$  and  $\text{PM}_{10}$  are within the range of 0.44–0.63 across all the mechanisms. The  $\text{SO}_2$  and  $\text{NO}_2$  have a range of 0.30–0.62, with CO and  $\text{O}_3$  ranging from 0.46 to 0.62. The strongest Pearson correlation was observed in the EWHHE simulations better than the PWPHHE. This agrees with previous studies conducted in this region (Fu et al., 2021a, 2023; Yabo et al., 2023). We observed from the outcome of the evaluation of the simulations that the simulated meteorological variables outperformed the air pollution variables, which effect could be noticed on how the EWHHE outperformed the PWPHHE. This could be attributed to uncertainties in the emission inventory (MEIC) due to a lack of available up-to-date data at the time of this experimental design. This might have contributed to the underestimation of air pollutants (Gao et al., 2016; Wang et al., 2019). Despite these uncertainties, our study demonstrated the model's trustworthiness and provided a baseline for additional sensitivity studies by accurately capturing the meteorological and chemical features of these significant air pollution events in future studies. Therefore, the model performance was consistent across all the radiative mechanisms, and the pollutants investigated were good.

### 3.2. Radiative mechanisms impacting UHI and UPII

The mechanisms influencing and altering the radiation budget through the processes of absorption and scattering of solar radiation are majorly attributed to aerosols. Aerosol radiative effects (AREs) are the mechanisms considered in this study that have been found to warm the atmosphere, cool surfaces, and impede the spread of contaminants in the PBL (Z. Li et al., 2017a). The ARE influences the increasing variations of aerosols between the urban and suburban/rural areas, which lower the solar radiation more in the urban centers than their rural counterparts. The urban and rural locations have variable aerosol loads and characteristics that tend to directly or indirectly impact UHII. ARE and aerosol dynamic effect (ADE) have been found to impact UHII (Han et al., 2020). The radiative mechanisms adopted in this study were the DRE, IRE, and SSE, with a default known as the NRE (see Table 2). In the subsequent subsections, we considered the spatial variations of these AREs on air pollutants (e.g.,  $\text{PM}_{2.5}$ ) and how it influences the changes in UPII and UHII (Fig. 5). During December 2019, the following dates and time (8th, 12,00, 12th, 06,00, 23rd, 12:00, 27th, 06:00) were selected to account for the EWHHE (Fig. 5 (a) – (p)), while the January 2020 dates and time (05th, 00,00, 09th, 12,00, 13th, 06,00, 28th, 06:00) to account for the PWPHHE (Fig. 5 (A) - (P)).

#### 3.2.1. Spatial variation of $\text{PM}_{2.5}$ and direct radiative effect (DRE) on UHI and UPII

The spatial variation of the  $\text{PM}_{2.5}$  was selected to account for the other air pollutants by demonstrating the impact of the DRE on UHII and UPII at different days and times of the months of the EWHHE and PWPHHE as shown in Fig. 5 (e – h) and (E – H), respectively. The  $\text{PM}_{2.5}$  concentration was low at the beginning of the winter with a value below  $100 \mu\text{g}/\text{m}^3$ , especially downtown, and its surroundings, as shown in the DRE (Fig. 5 (e) and (f)), which vary slightly with the NRE (Fig. 5 (a) and (b)). However, towards the end of the month, as shown in Fig. 5 (g) and (h)), the simulated  $\text{PM}_{2.5}$  concentration was observed to be  $>100 \mu\text{g}/\text{m}^3$ , which is similar to the NRE (Fig. 5 (c) and (d)). The air pollution persisted through PWPHHE, experiencing a low wind speed leading to the accumulation of air pollutants being transported towards the northwestern part of the domain (Fig. 5 (g) and (G)) and the southwesterly direction in Fig. 5 (h), (E), (F), and (H) from the downtown. We discovered that the spatial variation of the  $\text{PM}_{2.5}$  impacted by the DRE

had a similar pattern to that of the NRE, with just a slight variation during the different days and times. It has been reported from previous studies that incorporating only the DRE into the model influences  $\text{PM}_{2.5}$ , leading to the reduction in  $T_2$ , UHII, and surface upward and downward radiation mechanism (Makar et al., 2015b, a; Yabo et al., 2023). Generally, the spatial variation of the  $\text{PM}_{2.5}$  concentration was observed to be higher in the downtown, where emission sources are stronger than the surrounding satellite towns, which could influence the changes in UPII.

#### 3.2.2. Spatial variation of $\text{PM}_{2.5}$ and indirect radiative effect (IRE) on UHI and UPII

The IRE is one of the radiative mechanisms that interact with  $\text{PM}_{2.5}$ , which usually dominates the ARE compared to the DRE mechanism. The IRE was shown to be the dominant process in modifying atmospheric chemistry, which is consistent with the study by Wang et al. (2015). In this study, the IRE (shown in Fig. 5 (i - l) and (I – L)) is activated alongside the parameters of the DRE, which could be the possible reason for the dominance in the ARE. The impact demonstrated by the IRE was often shown to compete with the predictions of particulate matter, ozone, and other species (Makar et al., 2015a). The dominant effect of the IRE could be seen to be more pronounced in Fig. 5 (k), (l), and (I – L) when compared with those of its counterparts in the DRE and NRE. The  $\text{PM}_{2.5}$  concentrations influenced by its synergistic interactions with IRE could account for a value  $>200 \mu\text{g}/\text{m}^3$  in downtown Harbin than in its surrounding suburban/rural areas. The possible influential factors to this heavy pollution concentration have been attributed to low WS and due to stability in the PBL during the winter season (Ulpiani et al., 2021; Li et al., 2017b). We discovered generally that the WS was lower during the PWPHHE compared with days of low air pollution, whereby the WS was higher, especially at the beginning of the EWHHE.  $\text{PM}_{2.5}$  and other pollutants are majorly transported from the south to the north WD during the two episodes. The difference between the air pollution in the downtown with that of the suburban/rural counterparts influences the changes in UPII, which in turn impacts the air temperature variation leading to either UHII or UCII.

#### 3.2.3. Spatial variation of $\text{PM}_{2.5}$ with slope-and-shading effects (SSE) on UHI and UPII

The SSE mechanism was incorporated alongside the IRE to account for the impact of slope and shading effect interactions with radiative effect on air pollutants (such as  $\text{PM}_{2.5}$ ) and  $T_2$ . The SSE is topography dependent, which has some measure of impact on the meteorological variables and air pollutants related to the valley landform surrounded by the northern and southern mountains in the region (Wang et al., 2019). Our previous study was the first to introduce the SSE, which we discovered to have lowered UHII from the considerable difference between excellent and heavy pollution levels (Yabo et al., 2023). In this study, the SSE (shown in Fig. 5 (m) – (p) and (M) – (P)) has a similar spatial distribution pattern with the IRE. The little variation that could exist might be negligible in spatial form but could be noticeable when computed statistically. These changes could be a result of the influence of topography on the SSE, with the impact of meteorological fields and air pollution as contributing factors. The  $\text{PM}_{2.5}$  concentration is majorly centered within the core of the downtown with a maximum value  $>200 \mu\text{g}/\text{m}^3$ , which gradually reduces towards the suburban/rural areas having lesser concentration. The WS and WD have similar impacts on all the mechanisms found in the radiative effects considered in this study. Therefore, the spatial variation across all the radiative mechanisms could influence the changes in the UHII and UPII during the winter simulation in an area dominated by persistent air pollution, especially downtown Harbin.

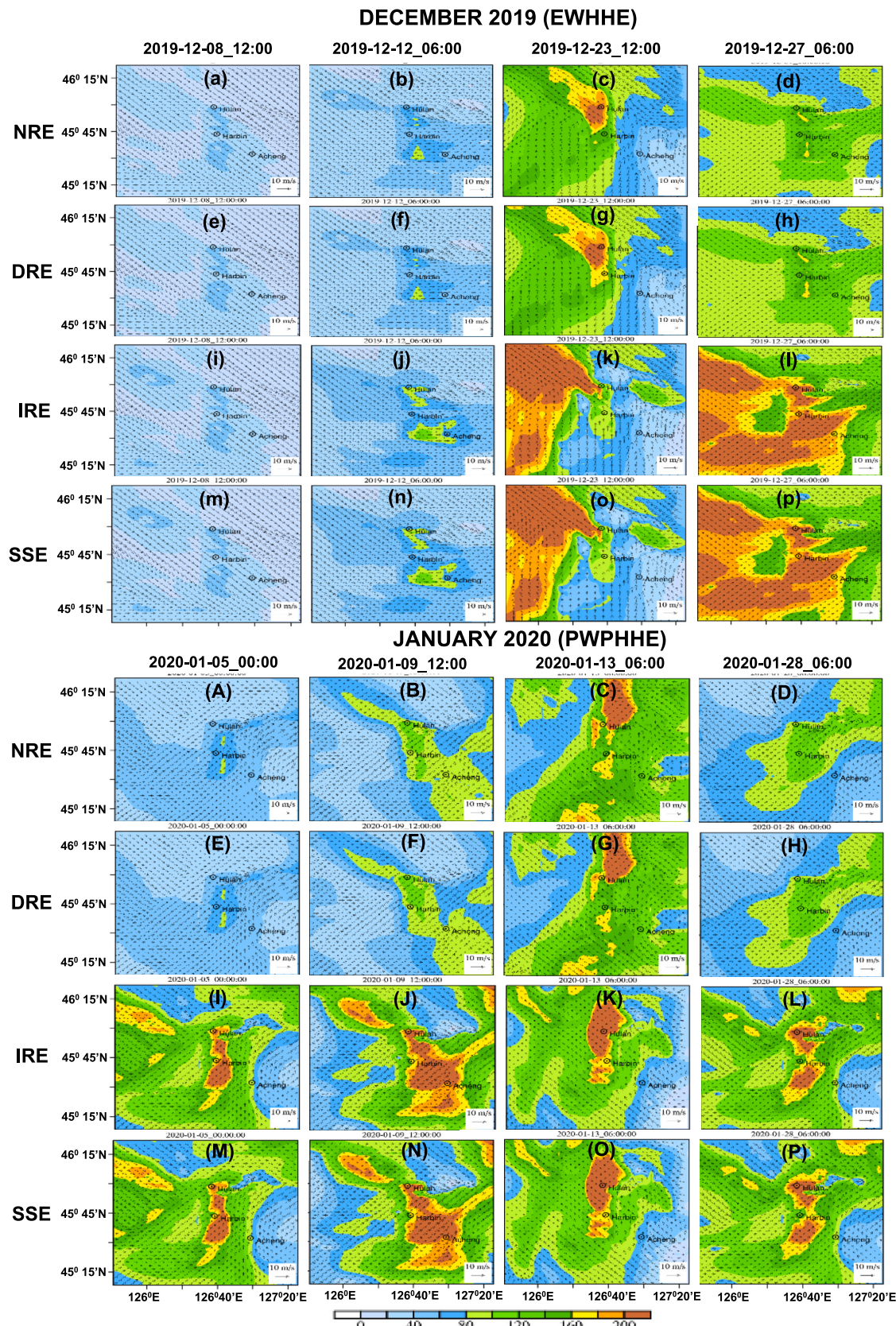


**Fig. 5.** Spatial variation of the different radiative mechanisms (NRE - (a - d) and (A - D), DRE - (e - h) and (E - H), IRE - (i - l) and (I - L), and SSE - (m - p) and (M - P)) and PM<sub>2.5</sub> concentrations influencing UHI and UPI. Note: December 2019 and January 2020 represent the early-winter-heavy-haze-episode (EWHHE) and peak-winter-persistent-heavy-haze-episode (PWPHHE), respectively.

### 3.3. Impact of radiative mechanisms and drivers on UHI and UPII with increasing pollution levels

#### 3.3.1. Urban stilling island intensity (USII; wind speed) influence on UHII and UPII

Wind speed (WS), as an important indicator of the wind field, is essential to many other climatic variables. WS is an indispensable part of urban climatology, affecting UHI and air pollution (Hou et al., 2013). The difference in WS between the urban and suburban/rural areas is known as the urban stilling island (USI) intensity (USII). In Fig. 6 (a) – (h), a comparison was made among three variables, namely, USII, UHII/UCII, and UPII. How these phenomena or variables interact and interrelate is crucial for understanding the influence of the different mechanisms employed in this study.

During the EWHHE (shown in Fig. 6 (a), (c), (e), and (g) corresponding to NRE, DRE, IRE, and SSE), the UHII progressively increases as the pollution moves from excellent to seriously polluted levels except at the good pollution level ( $35\text{--}75 \mu\text{g}/\text{m}^3$ ) where there is a slight decrease and the minimum value recorded at the NRE ( $0.04^\circ\text{C}$ ), IRE ( $0.11^\circ\text{C}$ ), and SSE ( $0.07^\circ\text{C}$ ). Similarly, in Table S4, the  $\text{NO}_2$  also experienced the same pattern as  $\text{PM}_{2.5}$  with the minimum value of the UHII of  $0.13^\circ\text{C}$  at the NRE, but the  $\text{PM}_{10}$  decrease at the moderately polluted level with the value of  $0.90^\circ\text{C}$  and  $0.93^\circ\text{C}$  for the IRE and SSE, respectively. Meanwhile, the UPII has a consistent increase from the excellent ( $< 35 \mu\text{g}/\text{m}^3$ ) to the seriously polluted ( $> 150 \mu\text{g}/\text{m}^3$ ) levels in the NRE ( $0.95 \mu\text{g}/\text{m}^3$  to  $77.48 \mu\text{g}/\text{m}^3$ ) and the DRE ( $0.85 \mu\text{g}/\text{m}^3$  to  $78.31 \mu\text{g}/\text{m}^3$ ), indicating that in winter, increase in UPII influences the changes in UHII at the early stage of the winter period due to the radiative effect (Wu et al., 2021; Yabo et al., 2023; Y. Yang et al., 2020b). However, the IRE (Fig. 6 (e)) and SSE (Fig. 6 (g)) impacted the UPII by lowering it at the good and slightly polluted levels for the  $\text{PM}_{2.5}$  with the minimum value recorded at  $-5.48 \mu\text{g}/\text{m}^3$  and  $-6.19 \mu\text{g}/\text{m}^3$ , respectively. Likewise, the  $\text{PM}_{10}$  and  $\text{NO}_2$ , which dominated the winter events like the  $\text{PM}_{2.5}$ , were found to maintain a consistent rise in the UPII from the excellent to seriously polluted levels, while the  $\text{SO}_2$ ,  $\text{CO}$ , and  $\text{O}_3$  have little impact in winter compared to the dominant pollutants. Comparatively, the USII defined based on Hou et al. (2013) driven by the WS with both UHII and UPII have a synergistic relationship and influence each other. From Fig. 6 ((a), (c), (e), and (g)), the USII was lowered at the excellent pollution level by  $-0.36 \text{ m/s}$ ,  $-0.33 \text{ m/s}$ ,  $-0.44 \text{ m/s}$ , and  $-0.42 \text{ m/s}$  for NRE, DRE, IRE, and SSE, respectively. Correspondingly, from Table S4, the  $\text{PM}_{10}$  had  $-0.40 \text{ m/s}$  (NRE),  $-0.35 \text{ m/s}$  (DRE),  $-0.43 \text{ m/s}$  (IRE), and  $-0.41 \text{ m/s}$  (SSE) while  $\text{NO}_2$  also has its excellent and good pollution levels for NRE ( $-0.5 \text{ m/s}$  and  $-0.33 \text{ m/s}$ ), DRE ( $-0.40 \text{ m/s}$  and  $-0.30 \text{ m/s}$ ), IRE ( $-0.46 \text{ m/s}$  each), and SSE ( $-0.46 \text{ m/s}$  and  $-0.43 \text{ m/s}$ ). The low values of USII revealed that the WS was higher in the downtown than in the satellite town, which tends to disperse air pollutants, hence resulting in excellent air quality. However, the maximum value of USII from each radiative effect for  $\text{PM}_{2.5}$  was recorded at moderately polluted level with values of  $0.91 \text{ m/s}$  (NRE) and  $0.95 \text{ m/s}$  (DRE) while at heavily polluted level with value of  $0.79 \text{ m/s}$  each for IRE and SSE, respectively. For  $\text{PM}_{10}$  and  $\text{NO}_2$  (Table S4), the maximum values of USII in all the radiative effects mechanisms were  $0.96 \text{ m/s}$  and  $0.92 \text{ m/s}$  (NRE),  $0.95 \text{ m/s}$  and  $0.93 \text{ m/s}$  (DRE),  $1.53 \text{ m/s}$  and  $0.90 \text{ m/s}$  (IRE), and  $1.27 \text{ m/s}$  and  $0.89 \text{ m/s}$  (SSE), which revealed that the rural WS is a dominant factor that influences the USII. At the heavily polluted level for  $\text{PM}_{2.5}$  (similar with  $\text{PM}_{10}$  and  $\text{NO}_2$ ; Table S4), the USII (NRE:  $0.79 \text{ m/s}$ ; DRE:  $0.85 \text{ m/s}$ ; IRE and SEE:  $0.79 \text{ m/s}$  each) favored the changes in UHII (NRE:  $1.42^\circ\text{C}$ ; DRE:  $1.35^\circ\text{C}$ ; IRE:  $1.66^\circ\text{C}$  and SSE:  $1.65^\circ\text{C}$ ) with increase in the UPII (NRE:  $77.48 \mu\text{g}/\text{m}^3$ ; DRE:  $78.31 \mu\text{g}/\text{m}^3$ ; IRE:  $94.18 \mu\text{g}/\text{m}^3$ ; SSE:  $95.59 \mu\text{g}/\text{m}^3$ ) during the EWHHE, thereby cause changes in UHII and UPII.

Considerably, during the PWPHHE (as shown in Fig. 6 (b), (d), (f), and (h) for radiative mechanisms NRE, DRE, IRE, and SSE, respectively), the UCII presents a unique phenomenon which describes the UHII with negative values where the peak winter temperature during this period

was slightly lower than its corresponding suburban/rural counterparts. The UCII continues to decrease as the  $\text{PM}_{2.5}$  concentration moves from excellent to heavily polluted levels, with the minimum values for each mechanism recorded at the heavily polluted level to be  $-2.14^\circ\text{C}$  (NRE),  $-2.29^\circ\text{C}$  (DRE),  $-1.45^\circ\text{C}$  (IRE), and  $-1.41^\circ\text{C}$  (SSE) while the maximum values for each radiative mechanism were recorded at the excellent pollution level as  $-0.87^\circ\text{C}$ ,  $-0.73^\circ\text{C}$ ,  $-0.69^\circ\text{C}$ , and  $-0.88^\circ\text{C}$  for NRE, DRE, IRE, and SSE, respectively. Similarly, the  $\text{NO}_2$  (Table S4) demonstrates the same pattern, with  $\text{PM}_{2.5}$  having the lowest UCII values recorded at the heavy pollution level and the maximum values at the excellent level for all the mechanisms, but  $\text{PM}_{10}$  varies slightly from these two pollutants. This indicates that extreme cold temperature and PHH are major contributors that influence the changes in the UCII. In the same vein, the UPII demonstrates the same pattern as the EWHHE, showing a consistent increase from excellent to heavy pollution levels, indicating that the air pollution in the downtown is higher than in the satellite town or suburban/rural counterparts. The minimum and maximum values of UPII according to each radiative mechanism of the  $\text{PM}_{2.5}$  are presented as NRE ( $3.73 \mu\text{g}/\text{m}^3$  and  $87.88 \mu\text{g}/\text{m}^3$ ), DRE ( $3.89 \mu\text{g}/\text{m}^3$  and  $82.77 \mu\text{g}/\text{m}^3$ ), IRE ( $-3.36 \mu\text{g}/\text{m}^3$  and  $78.39 \mu\text{g}/\text{m}^3$ ), and SSE ( $-2.98 \mu\text{g}/\text{m}^3$  and  $79.71 \mu\text{g}/\text{m}^3$ ). At the heavily polluted level for  $\text{PM}_{2.5}$ , the USII (NRE:  $0.10 \text{ m/s}$ ; DRE:  $0.22 \text{ m/s}$ ; IRE:  $0.24 \text{ m/s}$ ; SSE:  $0.23 \text{ m/s}$ ) lowered the changes in UCII (NRE:  $-2.14^\circ\text{C}$ ; DRE:  $-2.29^\circ\text{C}$ ; IRE:  $-1.45^\circ\text{C}$ ; SSE:  $-1.41^\circ\text{C}$ ) and UPII (NRE:  $87.88 \mu\text{g}/\text{m}^3$ ; DRE:  $82.77 \mu\text{g}/\text{m}^3$ ; IRE:  $78.39 \mu\text{g}/\text{m}^3$ ; SSE:  $79.71 \mu\text{g}/\text{m}^3$ ) during the PWPHHE with the USII lower than the EWHHE. Likewise, the  $\text{PM}_{10}$  and  $\text{NO}_2$  (shown in Table S4) also revealed a consistent increase in the UPII similar to the  $\text{PM}_{2.5}$  pollution levels. It was observed that the radiative mechanisms lowered the UPII, especially the heavy pollution level when compared with the NRE. Comparatively, the USII is a unique phenomenon that is triggered by the WS, especially the rural WS, which have their maximum values based on each mechanism as follows: NRE ( $0.30 \text{ m/s}$ ; at the good pollution level), DRE ( $0.28 \text{ m/s}$ ; at the slightly polluted level), while IRE ( $0.44 \text{ m/s}$ ) and SSE ( $0.37 \text{ m/s}$ ), both at the moderately polluted level. It is imperative to note that the accumulation and storage of air pollutants and heat are favored by low WS, while high WS helps in diffusing air pollutants and UHII during days of consistent winds (Alonso et al., 2007; Yang et al., 2021). Furthermore, a strong UHI case is characterized by low WS and high temperature. Low WSs are conducive to the coexistence of UHI with urban air pollution (Ulpiani, 2021). Our study in winter varies slightly with that of Yang et al. (2020a), which reported that UHII might dominate and decrease the USII under weaker large-scale wind in summer and autumn. It was also observed that the modeling of the topographic effect (SSE) on meteorological variables lowered winter speed (Wang et al., 2019), which further influence the changes in the USII, UHI, and UPII. Therefore, the USII favors the increase of UHII and UPII during the EWHHE but lowers the UCII during the PWPHHE with lower USII than the EWHHE.

#### 3.3.2. Urban dryness island intensity (UDII; relative humidity) influence on UHII and UPII

The urban dryness island intensity (UDII) is a phenomenon that compares the relative humidity (RH) of urban areas with that of suburban/rural areas (Yang et al., 2017). This important meteorological variable has been found to be lesser in cities than in their rural counterparts. The relationship that exists among UDII, UHII, and UPII for both EWHHE and PWPHHE are shown in Fig. 7 (a) – (h) and Table S5. How UDII varied uniquely in its interaction with the various radiative mechanisms employed in this study with UHII and UPII at different pollution levels is the goal of this section.

In particular, during the EWHHE (Fig. 7 (a), (c), (e), and (g)), the UHII and UPII have been observed to persistently increase from excellent to heavily polluted levels across the major air pollutants (such as  $\text{PM}_{2.5}$ ,  $\text{PM}_{10}$ ,  $\text{SO}_2$ ,  $\text{NO}_2$ ,  $\text{CO}$ , and  $\text{O}_3$ ). For the NRE and DRE (Fig. 7 (a) and (b)), the UDII varies at the  $\text{PM}_{2.5}$  levels with the maximum (6.62% and 6.12%) and minimum (3.35% and 3.40%) values recorded at both

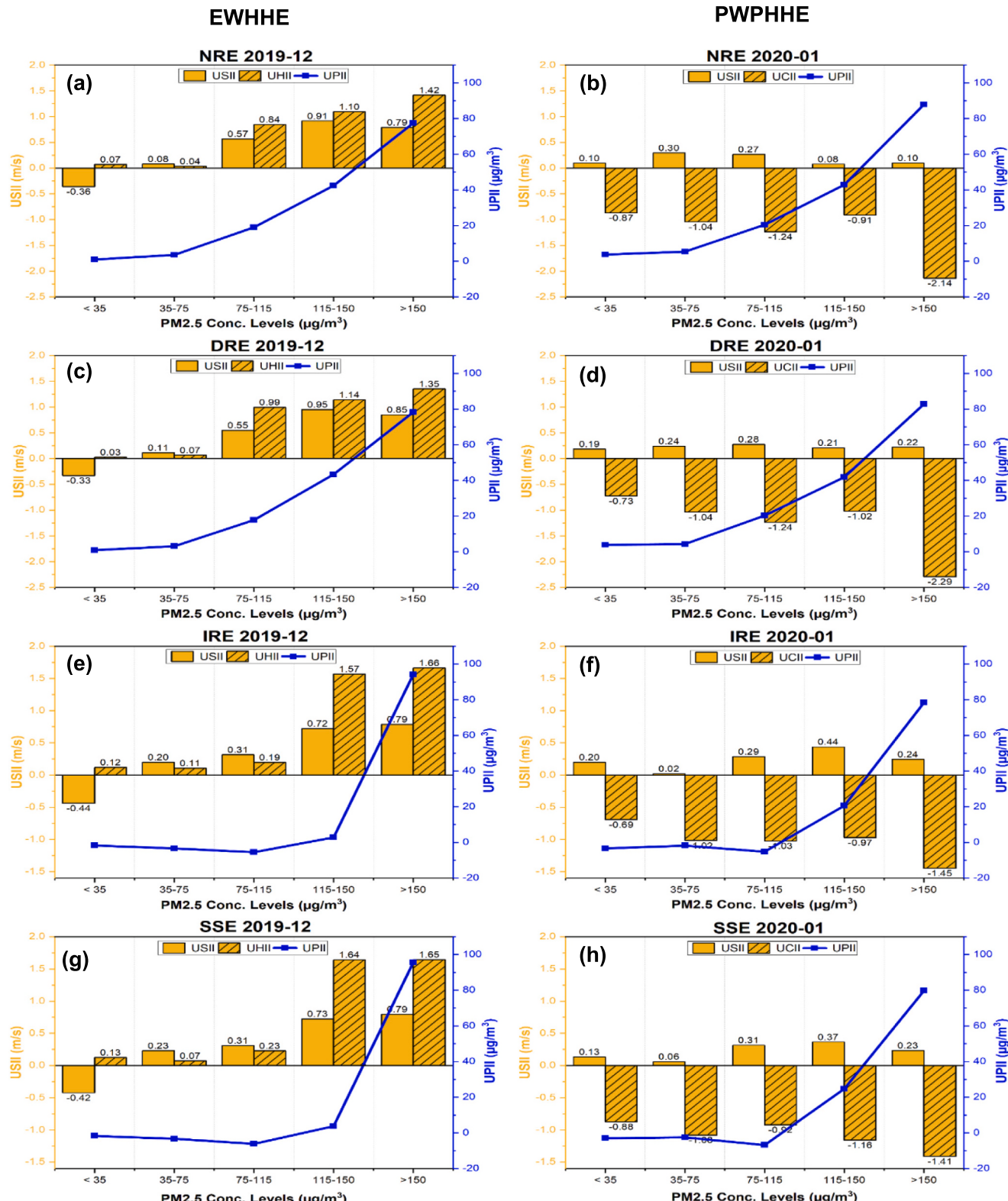


**Fig. 6.** Variations of the influence of urban stilling island intensity (USII; differences in wind speed between urban and sub-urban) on urban pollution island (UPI) and UHII with increasing PM<sub>2.5</sub> levels at different radiative mechanisms (NRE – (a) and (b), DRE – (c) and (d), IRE – (e) and (f); and SSE – (g) and (h)) during early winter heavy-haze episode (EWHHE) and peak winter persistent-heavy-haze episode (PWPHE).

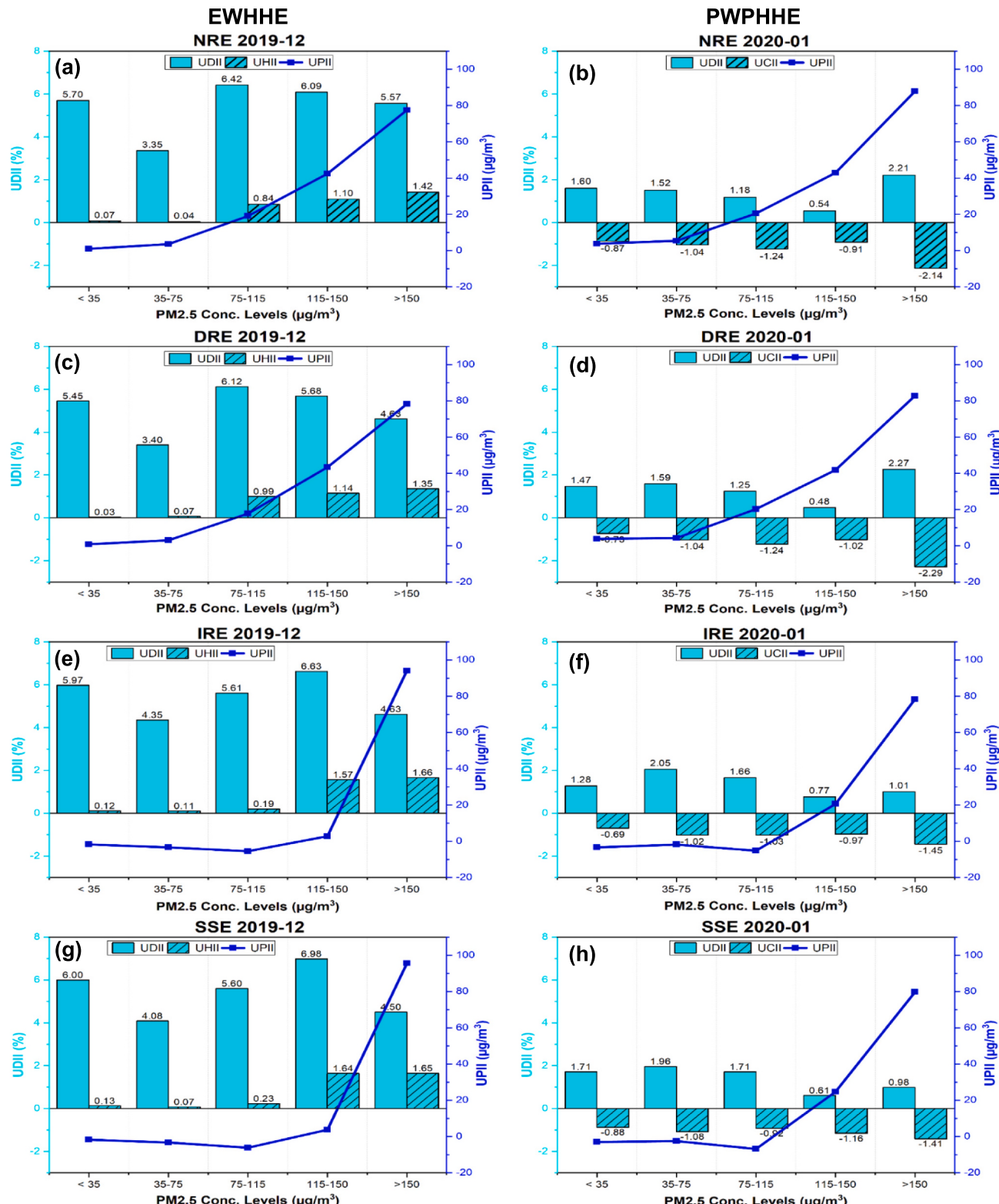


**Fig. 7.** Variations of the influence of urban dryness island intensity (UDII; differences in relative humidity between urban and suburban) on UPII and UHII with increasing PM<sub>2.5</sub> levels at different radiative mechanisms (NRE – (a) and (b), DRE – (c) and (d), IRE – (e) and (f), and SSE – (g) and (h)) during the early winter heavy-haze episode (EWHHE) and peak winter persistent-heavy-haze episode (PWPHE).

slightly polluted and good pollution levels, respectively. Meanwhile, the maximum value of UDII in IRE and SSE (Fig. 7 (e) and (g)) were observed at the moderately polluted PM<sub>2.5</sub> level with values of 6.63% and 6.98%, respectively, while the minimum values maintained the

same pollution level at the NRE and DRE. Similarly, from Table S5, the UDII of the PM<sub>10</sub> levels reveals that the slightly polluted level had the maximum values for each of the radiative mechanisms at NRE (6.06%), DRE (5.82%), IRE (6.02%), and SSE (6.16%). Meanwhile, the NO<sub>2</sub> had

the maximum value of UDII for each of the radiative mechanisms at the good pollution level to be 7.00% (NRE and IRE each), 6.24% (DRE), and 7.05% (SSE). Comparably, the UDII significantly impacted the interaction between the radiative mechanisms and the dominant pollutants ( $\text{NO}_2 > \text{PM}_{2.5} > \text{PM}_{10}$ ), with the highest UDII presented in the order greater than (>) at the SSE (7.05% > 6.98% > 6.16%), IRE (7.00% > 6.63% > 6.02%), NRE (7.00% > 6.42% > 6.02%), and DRE (6.24% > 6.12% > 5.82%) during the EWHHE, respectively. It is worth noting that among the other air pollutants,  $\text{NO}_2$  had the highest UDII at the SSE radiative effect, indicating that RH and UDII impacted the interaction between the  $\text{NO}_2$  and the radiative mechanisms more significantly than the other pollutants. Also, all the pollutants varied uniquely without a steady pattern of increase, like the UHII andUPII from the excellent to the heavily pollution levels.

In considering the PWPHE (Fig. 7(b), (d), (f), and (h)), the minimum value of the UDII for each of the radiative mechanisms was observed at the moderately polluted  $\text{PM}_{2.5}$  level with 0.54%, 0.48%, 0.77%, and 0.61% for NRE, DRE, IRE, and SSE, respectively. The maximum values of the UDII for NRE and DRE are 2.21% and 2.27%, both at the heavily polluted  $\text{PM}_{2.5}$  level, while that of IRE and SSE were observed at the good pollution level with values of 2.05% and 1.96%, respectively. As shown in Table S5, the maximum value of the UDII at the  $\text{PM}_{10}$  pollution level with 2.19% (NRE) and 1.92% (SSE) both at excellent pollution level, 3.00% (DRE; moderately polluted level), and 1.63% (IRE; good pollution level). Likewise, for the  $\text{NO}_2$ , the maximum value of the UDII for NRE (3.43%; excellent) with DRE (2.58%), IRE (2.53%), and SSE (2.78%) all recorded at a good pollution level, indicating that UDII does not necessarily thrive as UHII/UCII and UPII increases from excellent to heavily polluted levels, rather the impact is uniquely and particularly influenced by the pollution levels and radiative mechanisms with respect to the pollutants under investigation. Contrastingly, the UDII influenced the interaction between the radiative mechanisms and the dominant pollutants ( $\text{NO}_2 > \text{PM}_{2.5} > \text{PM}_{10}$ ), with the highest the highest UDII during the PWPHE at NRE (3.43% > 2.21% > 2.19%), SSE (2.78% > 1.96% > 1.92%), and IRE (2.53% > 2.05% > 1.63%), with only DRE in this order ( $\text{PM}_{10}$ : 3.00% >  $\text{NO}_2$ : 2.58%;  $\text{PM}_{2.5}$ : 2.27%), which were generally lower than the EWHHE. It has been highlighted that  $\text{SO}_2$ ,  $\text{CO}$ , and  $\text{O}_3$  have been observed to be very low in winter; therefore, we discussed only the dominant pollutants as they interact with UHII/UCII and UPII. Generally, we discovered that the UDII for the radiative mechanisms at the PWPHE were lower than the EWHHE, indicating that the peak winter lowers the activity of UDII (a by-product of RH) in the downtown, thereby, influencing the changes in the UHII and UPII. This was justified by the study of Yang et al. (2017) that UDII is weaker in winter and spring than in autumn and summer. Yang et al. (2017) further highlighted in the city of Beijing that the seasonal mean UDII is not the strongest nor the weakest in winter when considered with autumn, summer, and spring. This is because the RH and UDII are determined by both air temperature and atmospheric moisture. It could be deduced that urban development has a large impact on absolute physical variables like temperature and air pollution but not on RH and its phenomenon (UDII). Holmer and Eliasson (1999) revealed that a positive correlation existed between urban-rural RH differences and UHII, which consolidated our investigation that UDII has some measure of impact on UHII and UPII, especially during the heavy-haze events in downtown Harbin.

### 3.3.3. Urban planetary boundary layer height (UPBLH) intensity influence on UHII and UPII

The planetary boundary layer (PBL) exhibits double effects, one of which is known as the aerosol dynamic effect (ADE), a mechanism that stabilizes and maintains the airflow intensity by changing the thermodynamic structure (Han et al., 2020). In winter, it has been discovered that aerosols induced temperature inversion in the PBL, which provides a stable PBL that hampers the horizontal and vertical airflows and surface heat fluxes between the urban and suburban/rural areas (Li et al.,

2015; Z. Li et al., 2017a; Petäjä et al., 2016). The second effect exhibited by the PBL is being a meteorological driver, which is coined in this study as the urban planetary boundary layer height (UPBLH) intensity (UPBLHI), which is the difference between the urban and suburban/rural PBLH. The influence of the UPBLHI on UPII and UHII is described in Fig. 8(a) – (h) and Table S6 for both EWHHE and PWPHE.

Looking at the EWHHE (as shown in Fig. 8 (a), (c), (e), and (g) for NRE, DRE, IRE, and SSE, respectively), the UPBLHI varies at the different  $\text{PM}_{2.5}$  levels, which range from -37.14 m to 32.75 m (NRE), -22.56 m to 23.45 m (DRE), -7.82 m to 44.56 m (IRE), and -13.52 m to 48.07 m (SSE). The minimum values for the UPBLHI were all recorded at the excellent  $\text{PM}_{2.5}$  level for all the radiative mechanisms (NRE, DRE, IRE, and SSE), while the maximum values were observed at the slightly polluted levels (for NRE and DRE) and moderately polluted levels (for IRE and SSE). Similarly, for the  $\text{PM}_{10}$  and  $\text{NO}_2$  (Table S6), the minimum values were also recorded at the excellent pollution level with NRE (-27.64 m and -40.26 m), DRE (-19.15 m and -52.62 m), IRE and SSE (-31.10 m and -56.76 m; for only  $\text{NO}_2$ ) while at the seriously polluted level of  $\text{PM}_{10}$  for IRE and SSE (-18.18 m and -11.83 m), respectively, the relationship that exists between UPBLHI, UPII, and UHII varies as a result of the influence of the radiative mechanisms demonstrated in NRE, DRE, IRE, and SSE. The PBLH is very low in winter as a result of increasing pollutant concentration, which has been attributed to high emissions leading to PHH episodes (Petäjä et al., 2016). We discovered in winter that as the UPII increased from an excellent pollution level to a heavily polluted level, the UPBLHI was lowered with a slight increase in the UHII, especially during the EWHHE.

In considering the PWPHE (Fig. 8 (b), (d), (f), and (h)), we observed that the PBLH was lower than the EWHHE, resulting in low UPBLHI which could be attributed to the persistent pollution episode. The range of values of the UPBLHI impacted by the radiative mechanisms is as follows: NRE (-12.15 m to 20.86 m), DRE (-4.45 m to 18.60 m), IRE (-7.28 m to 15.56 m), and SSE (-11.28 m to 10.00 m) with the maximum values recorded at the NRE and DRE, while the minimum values for IRE and SSE were all at the heavily polluted level. Likewise, for the  $\text{PM}_{10}$  and  $\text{NO}_2$  (Table S6), the minimum values of UPBLHI for  $\text{PM}_{10}$  observed at the good pollution level were -0.54 m (NRE) and -1.42 m (DRE), and at moderately polluted level was -3.65 m and -5.30 m for IRE and SSE, respectively. At the same time, the  $\text{NO}_2$  was recorded at the slightly polluted level for NRE (-3.48 m), DRE (-3.20 m), IRE (-4.40 m), and SSE (-4.69 m). Besides, the maximum value of the UPBLHI for  $\text{PM}_{10}$  recorded at slightly polluted levels were 18.64 m (NRE) and 20.63 m (DRE), and at the good pollution levels were 11.24 m (IRE) and 13.12 m (SSE), while for  $\text{NO}_2$  were 21.86 m, 18.75 m, and 21.50 m for NRE, DRE, and IRE, respectively. Moreover, at the heavily polluted level for  $\text{NO}_2$ , the maximum value of the UPBLHI was 43.50 m for the SSE. This was a result of the lowered PBLH being impacted by the radiative mechanisms and high pollution concentration, which reduces the amount of solar radiation reaching the earth's surface. Comparably, we discovered that the UPBLHI was generally lower during the PWPHE than the EWHHE, with a maximum value of the  $\text{NO}_2$  (SSE: 43.50 m < 52.57 m),  $\text{PM}_{2.5}$  (NRE: 18.60 m < SSE: 48.07 m), and  $\text{PM}_{10}$  (DRE: 20.63 m < IRE: 30.37 m). The study by Han et al. (2020) further asserts that heat exchange and pollution dispersion within the PBL are weakened in polluted conditions due to a decrease in both horizontal and vertical exchanges (a summary of our results can be found in Table S7). Also, the strongest interactions between meteorological variables and aerosols usually take place in the PBL, which are affected by AREs (Yu et al., 2002; Li et al., 2017b). Specifically, the topographic effect (for example, SSE) on meteorological variables related to this study area with the lowered PBLH has more intense temperature inversion (Wang et al., 2019), which exerts some influence on UHII and UPII. During the PWPHE, the UCII is very low, with all values negative at all the pollution levels, which has been attributed to low PBLH and radiative effects resulting from the increase in high pollutant concentrations. Gao

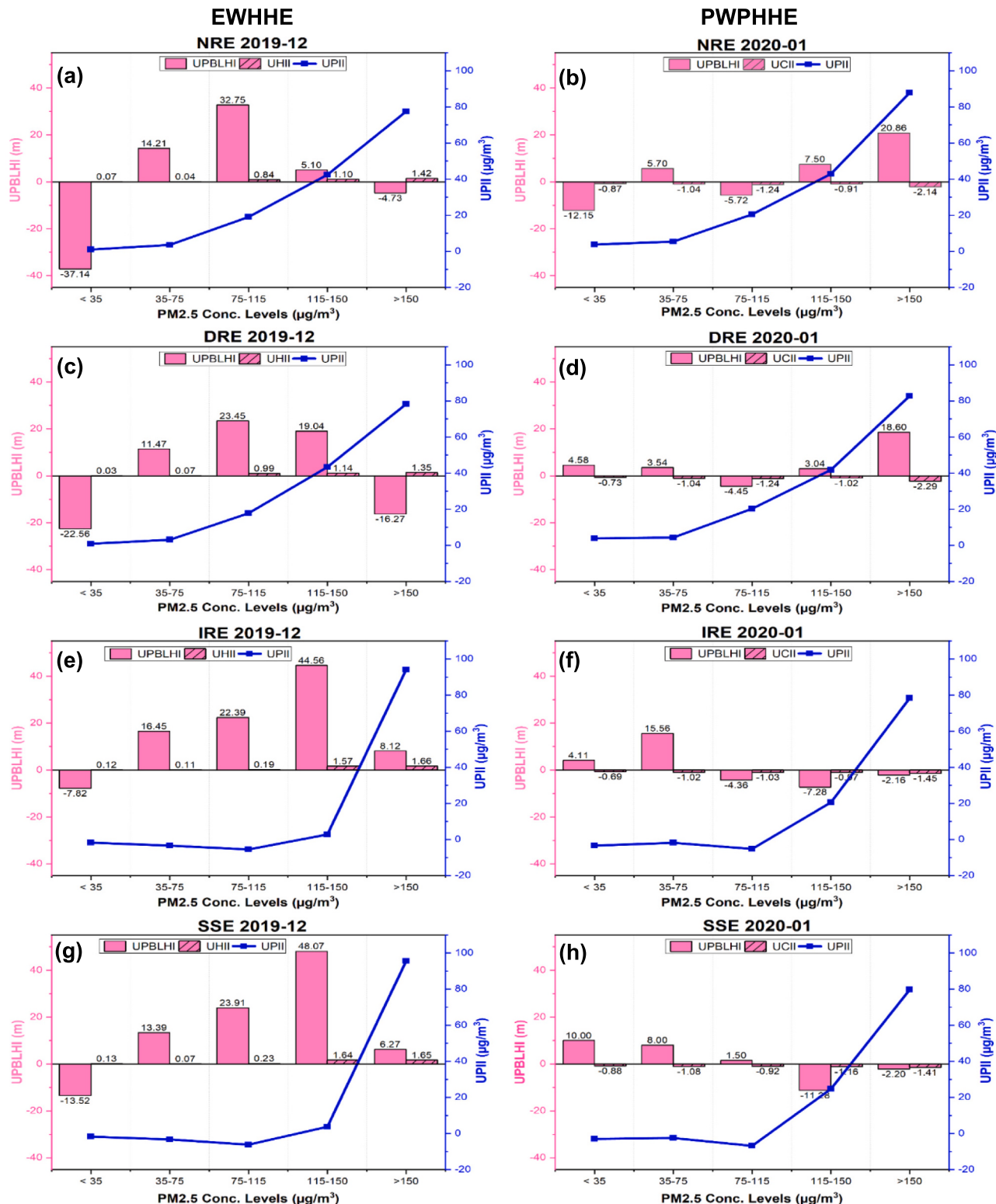


**Fig. 8.** Variations of the influence of urban Planetary boundary layer height (UPBLH) island intensity (differences in Planetary boundary layer height between urban and sub-urban) on urban pollution island (UPI) and UHII with increasing PM<sub>2.5</sub> levels at different radiative mechanisms (NRE – (a) and (b), DRE – (c) and (d), IRE – (e) and (f); and SSE – (g) and (h)) during the early winter heavy-haze episode (EWHHE) and peak winter persistent-heavy-haze episode (PWPHHE).

et al. (2023) also affirm that aerosols increase atmospheric stability by inducing a temperature inversion due to the absorption and scattering of solar radiation, which hinders the dispersion of pollutants (see Table S7). Therefore, UPBLHI is a major meteorological variable that cannot be ignored in the interactions with UPII and UHII/UCII, which

plays a significant role in the changing of UHII in winter, especially during PHH events.

### 3.3.4. Influence of wind direction and speed on UHII and UPII at different wind speed levels

The influence of wind direction (WD) on UHII and UPII is in synergy with WS, which is a major meteorological factor that influences the changes during EWHHE and PWPHE. The WD has been reported to be a key factor in the variation of PM<sub>2.5</sub> (Chen et al., 2020). The inter-city and regional transport of air pollutants during high pollution episodes are influenced by WD and WS alongside other factors that are not considered in this section. Therefore, how WD, in synergy with WS, influences UHII and UPII through the different radiative mechanisms is vital for our understanding of the mechanisms and drivers involved in the interactions among the various phenomena considered during the EWHHE and PWPHE in the downtown and the suburban areas.

During the EWHHE (Fig. 9 (a), (b), (e), and (f)), the WD dominating downtown Harbin in all the mechanisms were the southwesterly and northwesterly winds (clockwise) with the maximum percentage frequency recorded at approximately 22% (WNW) while the dominant WD in the Acheng satellite town were from direct southern towards the northwestern direction (clockwise) with the maximum percentage frequency 18% (S). How WD influences the concentrations of air pollutants in downtown Harbin and its surroundings is highly dependent on local geographical conditions and possibly the distribution of pollutants concentration, which makes the region quite unique to any other place in China. We discovered in this study that the weaker northerly winds substantially contribute to the increase in the pollutant concentration in Northeast China. This was also affirmed in the North China Plain (NCP) by Yang et al. (2016). In all the mechanisms during the EWHHE, the highest concentration of pollutants (for example, PM<sub>2.5</sub>) was recorded at the lowest WS level (0–2 m/s), with the highest value of the PM<sub>2.5</sub> concentration of 206.43 µg/m<sup>3</sup> recorded at IRE for Harbin and 139.25 µg/m<sup>3</sup> at SSE for the Acheng satellite town. The average value of UPII at the lowest WS level (0–2 m/s) for the different mechanisms were 44.00 µg/m<sup>3</sup> (NRE), 48.47 µg/m<sup>3</sup> (DRE), 73.04 µg/m<sup>3</sup> (IRE), and 65.59 µg/m<sup>3</sup> (SSE). The possible reason why the IRE has the highest UPII could be inferred from the combined effects of both the direct and indirect aerosols radiative effect (from our previous study by Yabo et al. (2023), which is also asserted by the study of Makar et al. (2015a). We

discovered in this study that higher WS lowers the pollutant's concentration while lower WS leads to the high concentration of air pollutants in a particular WD, which is aided by the different aerosol radiative mechanisms. A possible reason could be that the change in WD from the south to the north has been reported to enhance persistent haze episodes (Shi et al., 2020). Similarly, the WD and WS enhance the changes in UHII with the maximum positive values dominating the 2–4 m/s WS level in the order at 2.15 °C (IRE) > 2.13 °C (NRE) > 2.10 °C (SSE) > 2.03 °C (DRE) for each of the mechanisms. Likewise, the minimum value of the UHII for each of the mechanisms at NRE (−7.40 °C), DRE (−5.62 °C), IRE (−5.61 °C), and SSE (−5.28 °C), which dominate the highest (8–10 m/s) WS level. Hence, this reveals that low WS and the south-to-north WD have a significant impact on UHII due to low temperature and the influence of the mechanisms.

In the PWPHE (Fig. 9 (c), (d), (g), and (h) corresponding to the mechanisms NRE, DRE, IRE, and SSE, respectively), the WD in the downtown Harbin is dominated by the southwesterly winds with a maximum percentage frequency recorded at 16% (WSW) while Acheng had 15% (S) dominated by the southerly winds. The PM<sub>2.5</sub> concentration at downtown Harbin majorly dominated the 0–2 m/s WS level, while Acheng is dominated by 2–4 m/s WS level for all the mechanisms except for the NRE, which slightly increases at the different WS levels. The maximum PM<sub>2.5</sub> concentration for downtown Harbin was recorded at IRE (153.63 µg/m<sup>3</sup>), while the Acheng was recorded at SSE (104.72 µg/m<sup>3</sup>) and is similar to EWHHE. The UPII maximum average value shown at 0–2 m/s WS level (during the PWPHE) for each of the mechanisms at NRE (32.72 µg/m<sup>3</sup>), IRE (49.18 µg/m<sup>3</sup>), and SSE (48.09 µg/m<sup>3</sup>) while DRE (25.46 µg/m<sup>3</sup>) was at 4–6 m/s WS level. The highest value of UPII was observed at the IRE, followed by the SSE, which could be due to the aerosol radiative mechanism dominating the IRE and SSE, which was highlighted in our previous study (Yabo et al., 2023). Likewise, low WS also stabilizes the PBLH, which leads to high air pollutant concentrations (Alonso et al., 2007; Yang et al., 2021). Moreover, the UHII influenced by the WD and WS has its average maximum value at 4–6 m/s WS level for each of the mechanisms were NRE (2.24 °C), DRE (2.17 °C), IRE (2.62 °C), and SSE (2.30 °C). The IRE had the highest value of the UHII in both EWHHE and PWPHE, inferring the impact of aerosols in

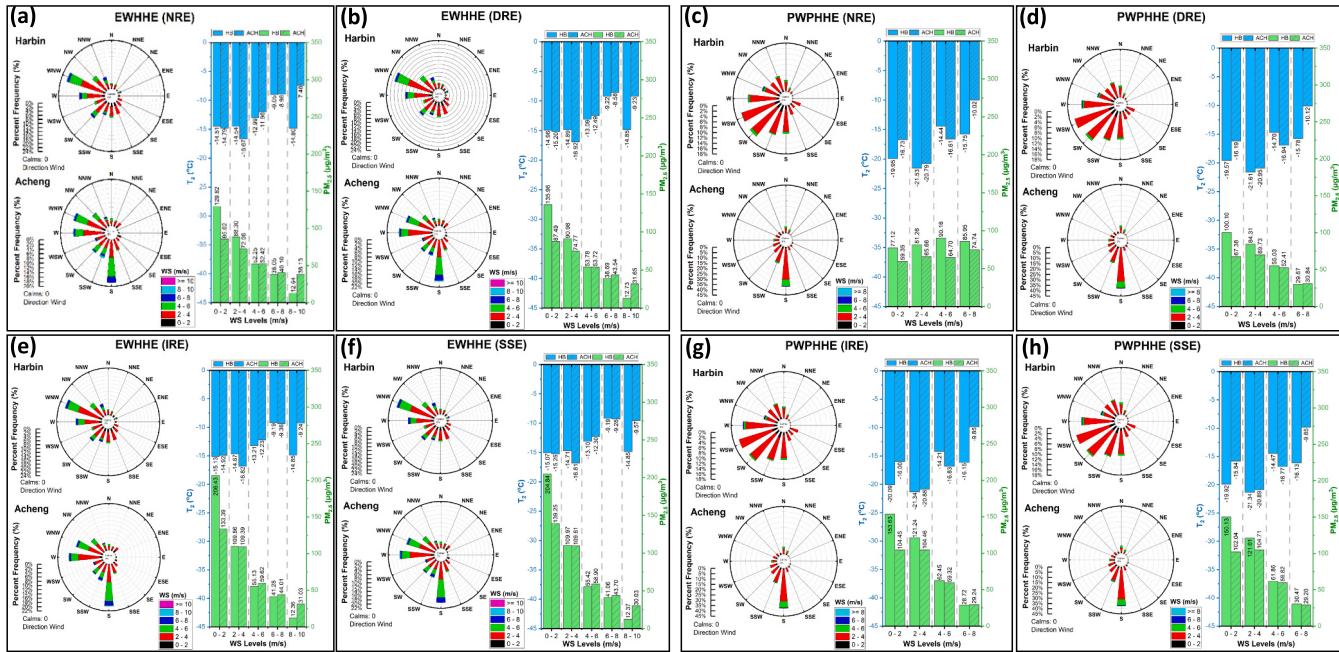


**Fig. 9.** Variations of the influence of wind direction (WD) and wind speed (WS) on urban pollution island intensity (UPII) and urban heat island intensity (UHII) with increasing WS levels at different radiative mechanisms (NRE – (a) and (c), DRE – (b) and (d), IRE – (e) and (g), and SSE – (f) and (h)) during the early winter heavy-haze episode (EWHHE) and peak winter persistent-heavy-haze episode (PWPHE).

dominating the indirect effect, which was also confirmed to deteriorate winter haze in the NCP (Wu et al., 2019; see summary from Table S7), hence leading to a significant impact on UHII. Therefore, the change in WD from the south to north influenced by WS led to persistent haze episodes, which in turn impacted the UPII and UHII/UCII in Harbin, a cold megacity in Northeast China.

#### 4. Conclusion and limitations

The Northeastern part of China, especially Harbin has experienced prevalent problems of persistent-heavy-haze events and extreme-cold temperatures during the prolonged winter season, which has led to numerous environmental problems, with special consideration on urban heat/cold island and urban pollution island in this study, during the early winter heavy-haze episode (EWHHE; December 2019) and peak winter persistent-heavy-haze episode (PWPHE; January 2020). This study demonstrates the importance of including various radiative mechanisms and novel drivers for understanding urban climate and air pollution studies under heavy-haze conditions. A high-resolution WRF-Chem model was utilized to probe into the various radiative mechanisms and drivers influencing the phenomena of urban heat-cold island intensity (UHII/UCII) and urban pollution island intensity (UPII). As a whole, the model accurately replicates the spatial distributions of the mass concentrations of PM<sub>2.5</sub>, PM<sub>10</sub>, SO<sub>2</sub>, NO<sub>2</sub>, CO, and O<sub>3</sub> and meteorological variables (T<sub>2</sub>, RH, WS, and WD) as against the observation data for proper validation.

The outcomes of this study and major conclusions are summarized as follows:

- High aerosol loads (especially the PM<sub>2.5</sub>) are mainly distributed in the downtown which is dominated by residential emission sources rather than its surrounding satellite towns, thereby influencing the changes in UHII and UPII.
- Spatially, the IRE and the SSE dominated the aerosol radiative effects with PM<sub>2.5</sub> concentrations accounting for >200 µg/m<sup>3</sup> in both EWHHE and PWPHE.

The impact of the various radiative mechanisms and drivers was examined to account for the changes in UHII and UPII during the EWHHE and PWPHE;

- We discovered that at the heavily polluted level for the PM<sub>2.5</sub> (similar to the PM<sub>10</sub> and NO<sub>2</sub> in Table S4) of the different ARE, the USII (NRE: 0.79 m/s; DRE: 0.85 m/s; IRE and SEE: 0.79 m/s each) influenced the changes in UHII (NRE: 1.42 °C; DRE: 1.35 °C; IRE: 1.66 °C and SSE: 1.65 °C) by increasing the UPII (NRE: 77.48 µg/m<sup>3</sup>; DRE: 78.31 µg/m<sup>3</sup>; IRE: 94.18 µg/m<sup>3</sup>; SSE: 95.59 µg/m<sup>3</sup>) during the EWHHE, but lowered the UCII (NRE: -2.14 °C; DRE: -2.29 °C; IRE: -1.45 °C; SSE: -1.41 °C) and UPII (NRE: 87.88 µg/m<sup>3</sup>; DRE: 82.77 µg/m<sup>3</sup>; IRE: 78.39 µg/m<sup>3</sup>; 79.71 µg/m<sup>3</sup>) during the PWPHE, with the USII (NRE: 0.10 m/s; DRE: 0.22 m/s; IRE: 0.24 m/s; SSE: 0.23 m/s) lower than the EWHHE. The suburban/rural wind speed (WS) was the dominant factor that influenced the USII.
- The UDII significantly impacted the interaction between the radiative mechanisms and the dominant pollutants (NO<sub>2</sub> > PM<sub>2.5</sub> > PM<sub>10</sub>), with the highest UDII presented at the SSE (7.05% > 6.98% > 6.16%), IRE (7.00% > 6.63% > 6.02%), NRE (7.00% > 6.42% > 6.02%), and DRE (6.24% > 6.12% > 5.82%) during the EWHHE, respectively. Likewise, the UDII during the PWPHE at NRE (3.43% > 2.21% > 2.19%), SSE (2.78% > 1.96% > 1.92%), and IRE (2.53% > 2.05% > 1.63%), with only DRE in this order (PM<sub>10</sub>: 3.00% > NO<sub>2</sub>: 2.58%; PM<sub>2.5</sub>: 2.27%), which were generally lower than the EWHHE. Therefore, we found that the PWPHE lowers the activity of UDII in the downtown than the EWHHE by influencing the changes in the UHII and UPII.

• Moreover, we discovered that the UPBLHI was generally lower during the PWPHE than the EWHHE, with a maximum value of the NO<sub>2</sub> (SSE: 43.50 m < 52.57 m), PM<sub>2.5</sub> (NRE: 18.60 m < SSE: 48.07 m), and PM<sub>10</sub> (DRE: 20.63 m < IRE: 30.37 m), revealing that high pollutant concentration leads to persistent heavy-haze, which lowers the PBLH by increasing atmospheric stability, hence, impacts the UHII/UCII and UPII. Also, the strongest interactions between meteorological variables and aerosols usually take place in the PBL, which are affected by the radiative effect mechanisms.

• Furthermore, we also found that WD influences the concentration of air pollutants by weakening the northerly winds, which plays a significant role in enhancing the pollutant concentration in downtown Harbin and its surroundings. The IRE had the highest value of the UPII in both EWHHE and PWPHE, inferring the impact of aerosols in dominating the radiative mechanisms, leading to a significant impact on UHII. The changes in WD from the south to north influenced by WS led to persistent haze episodes, which in turn impacted the UPII and UHII in a cold megacity of Northeast China.

Generally, the radiative mechanisms and novel drivers influencing the changes in the USII, UDII, and UPBLHI phenomena tend to cause variations in the UHII and UPII at the different pollution levels in both episodes. The USII, UDII, and UPBLHI (by-products of WS, RH, and PBLH) with WD are major contributors to the high concentration of air pollutants in the cold region. Also, the modeling revealed a slight impact of the SSE on meteorological variables due to topographic effects, which lowered PBLH and reduced WS during the PHH. Our study varies significantly from previous studies as a result of the concepts used (see Table S7 for the summary). This work has improved our understanding of urban climate and air quality studies by providing a scientific basis for the mechanisms and drivers influencing the synergy between UHII and UPII. Also, it should provide a significant precursor for other urban areas with severe air pollution. Although, the limitation of modeling simulations of aerosol radiative mechanisms was impacted by the uncertainties from regional meteorological fields and the emission inventory, therefore, up-to-date datasets with better resolution are necessary in order to minimize these uncertainties and improve the model's performance. Future studies should be conducted to account for the impact of other radiative mechanisms, drivers, and full-scale topographic effects on UHII and UPII during haze pollution.

#### CRediT authorship contribution statement

**Stephen Dauda Yabo:** Conceptualization, Data curation, Formal analysis, Methodology, Writing – original draft, Writing – review & editing. **Lu Lu:** Resources, Validation, Visualization. **Lixin Ma:** Investigation, Validation. **Bo Li:** Resources, Software. **Donglei Fu:** Resources, Software. **Fan Meng:** Investigation, Visualization. **Jinpan Jiang:** Investigation, Resources. **Xie Shengjin:** Resources. **Wei Zhang:** Formal analysis, Methodology, Resources, Validation. **Hong Qi:** Conceptualization, Funding acquisition, Methodology, Project administration, Resources, Supervision, Writing – review & editing.

#### Declaration of competing interest

The authors declare that they have no known competing financial interests or personal relationships that could have appeared to influence the work reported in this paper.

#### Data availability

Data will be made available on request.

#### Acknowledgements

This study was supported by the Open Project of the State Key

Laboratory of Urban Water Resource and Environment, Harbin Institute of Technology (No. HC202143), and the Heilongjiang Provincial Key Laboratory of Polar Environment and Ecosystem (HPKL-PEE) (No. 2021011).

## Appendix A. Supplementary data

Supplementary data to this article can be found online at <https://doi.org/10.1016/j.atmosres.2024.107259>.

## References

- Ackerman, B., Changnon, S., Dzurisin, G., 1978. Summary of METROMEX, volume 2: causes of precipitation anomalies. *Urbania* 399.
- Ackermann, I.J., Hass, H., Memmesheimer, M., Ebel, A., Binkowski, F.S., Shankar, U., 1998. Modal aerosol dynamics model for Europe: development and first applications. *Atmos. Environ.* 32, 2981–2999. [https://doi.org/10.1016/S1352-2310\(98\)00006-5](https://doi.org/10.1016/S1352-2310(98)00006-5).
- Alonso, M.S., Fidalgo, M.R., Labajo, J.L., 2007. The urban heat island in Salamanca (Spain) and its relationship to meteorological parameters. *Clim. Res.* 34, 39–46. <https://doi.org/10.3354/cr034039>.
- Bei, N., Wu, J., Elser, M., Feng, T., Cao, J., El-Haddad, I., Li, X., Huang, R., Li, Z., Long, X., Xing, L., Zhao, S., Tie, X., Prévôt, A.S.H., Li, G., 2017. Impacts of meteorological uncertainties on the haze formation in Beijing-Tianjin-Hebei (BTH) during wintertime: a case study. *Atmos. Chem. Phys.* 17, 14579–14591. <https://doi.org/10.5194/acp-17-14579-2017>.
- Boylan, J.W., Russell, A.G., 2006. PM and light extinction model performance metrics, goals, and criteria for three-dimensional air quality models. *Atmos. Environ.* 40, 4946–4959. <https://doi.org/10.1016/j.atmosenv.2005.09.087>.
- Chakraborty, T., Sarangi, C., Tripathi, S.N., 2017. Understanding Diurnality and Inter-Seasonality of a Sub-tropical Urban Heat Island. *Boundary-Layer Meteorol.* 163, 287–309. <https://doi.org/10.1007/s10546-016-0223-0>.
- Chen, F., Dudhia, J., 2001. Coupling and advanced land surface-hydrology model with the Penn State-NCAR MM5 modeling system. Part I: model implementation and sensitivity. *Mon. Weather Rev.* 129, 569–585. [https://doi.org/10.1175/1520-0493\(2001\)129<0569:CAALSH>2.0.CO;2](https://doi.org/10.1175/1520-0493(2001)129<0569:CAALSH>2.0.CO;2).
- Chen, Q., Yuan, Y., Huang, X., He, Z., Tan, H., 2018b. Assessment of column aerosol optical properties using ground-based sun-photometer at urban Harbin, Northeast China. *J. Environ. Sci. (China)* 74, 50–57. <https://doi.org/10.1016/j.jes.2018.02.003>.
- Chen, Z., Xie, X., Cai, J., Chen, D., Gao, B., He, B., Cheng, N., Xu, B., 2018a. Understanding meteorological influences on PM2.5 concentrations across China: a temporal and spatial perspective. *Atmos. Chem. Phys.* 18, 5343–5358. <https://doi.org/10.5194/acp-18-5343-2018>.
- Chen, Z., Chen, D., Zhao, C., Kwan, M., Po, Cai, J., Zhuang, Y., Zhao, B., Wang, X., Chen, B., Yang, J., Li, R., He, B., Gao, B., Wang, K., Xu, B., 2020. Influence of meteorological conditions on PM2.5 concentrations across China: a review of methodology and mechanism. *Environ. Int.* 139, 105558 <https://doi.org/10.1016/j.envint.2020.105558>.
- Cheng, Y., Cao, X., Bing, Yu, Q., Qin, Liu, J., Meng, Ma, W., Li, Qi, H., Zhang, Q., He, K., Bin, 2022. Synergy of multiple drivers leading to severe winter haze pollution in a megacity in Northeast China. *Atmos. Res.* 270, 106075 <https://doi.org/10.1016/j.atmosres.2022.106075>.
- Chou, M.-D., Suarez, M.J., Liang, X.-Z., Yan, M.M.H., Cote, C., 2001. A thermal infrared Radiation Parameterization for Atmospheric Studies. In: NASA Technical Report Series on Global Modeling and Data Assimilation, p. 19.
- Chylek, P., Wong, J., 1995. Effect of absorbing aerosols on global radiation budget. *Geophys. Res. Lett.* 22, 929–931. <https://doi.org/10.1029/95GL00800>.
- Crutzen, P.J., 2004. New Directions: The growing urban heat and pollution “island” effect - Impact on chemistry and climate. *Atmos. Environ.* 38, 3539–3540. <https://doi.org/10.1016/j.atmosenv.2004.03.032>.
- Cui, L., Shi, J., 2012. Urbanization and its environmental effects in Shanghai, China. *Urban Clim* 2, 1–15. <https://doi.org/10.1016/j.uclim.2012.10.008>.
- Ding, L., Zhu, D., Peng, D., Zhao, Y., 2017. Air pollution and asthma attacks in children: a case-crossover analysis in the city of Chongqing, China. *Environ. Pollut.* 220, 348–353. <https://doi.org/10.1016/j.envpol.2016.09.070>.
- Du, C., Liu, S., Yu, X., Li, X., Chen, C., Peng, Y., Dong, Y., Dong, Z., Wang, F., 2013. Urban boundary layer height characteristics and relationship with particulate matter mass concentrations in Xi'an, Central China. *Aerosol Air Qual. Res.* 13, 1598–1607. <https://doi.org/10.4209/aaqr.2012.10.0274>.
- EEA, 2011. The application of models under the European Union's Air Quality Directive: A Technical Reference Guide. In: European Environment Agency Technical. Report No 10/2011.
- Fast, J.D., Gustafson, W.I., Easter, R.C., Zaveri, R.A., Barnard, J.C., Chapman, E.G., Grell, G.A., Peckham, S.E., 2006. Evolution of ozone, particulates, and aerosol direct radiative forcing in the vicinity of Houston using a fully coupled meteorology-chemistry-aerosol model. *J. Geophys. Res. Atmos.* 111, 1–29. <https://doi.org/10.1029/2005JD006721>.
- Fu, D., Shi, X., Xing, Y., Wang, P., Li, H., Li, B., Lu, L., Thapa, S., Yabo, S., Qi, H., Zhang, W., 2021a. Contributions of extremely unfavorable meteorology and coal-heating boiler control to air quality in December 2019 over Harbin, China. *Atmos. Pollut. Res.* 12, 1–10. <https://doi.org/10.1016/j.apr.2021.101217>.
- Fu, D., Zhang, W., Xing, Y., Li, H., Wang, P., Li, B., Shi, X., Zuo, J., Yabo, S., Thapa, S., Lu, L., Qi, H., Ma, J., 2021b. Impacts of maximum snow albedo and land cover changes on meteorological variables during winter in Northeast China. *Atmos. Res.* <https://doi.org/10.1016/j.atmosres.2021.105449>.
- Fu, D., Shi, X., Zuo, J., Yabo, S.D., Li, J., Li, B., Li, H., Lu, L., Tang, B., Qi, H., Ma, J., 2023. Why did air quality experience little improvement during the COVID-19 lockdown in megacities, Northeast China? *Environ. Res.* 221 <https://doi.org/10.1016/j.envr.2023.115282>.
- Gao, L., Wang, T., Ren, X., Ma, D., Qu, Y., Wu, H., 2023. Mechanism of persistent heavy PM2.5 pollution over the Beijing-Tianjin-Hebei region of China: a combination of aerosol radiative effect and atmospheric quasi-biweekly oscillation. *Atmos. Environ.* 303, 119751 <https://doi.org/10.1016/j.atmosenv.2023.119751>.
- Gao, M., Carmichael, G.R., Wang, Y., Saide, P.E., Yu, M., Xin, J., Liu, Z., Wang, Z., 2016. Modeling study of the 2010 regional haze event in the North China Plain. *Atmos. Chem. Phys.* 16, 1673–1691. <https://doi.org/10.5194/acp-16-1673-2016>.
- Giannaros, T.M., Melas, D., Daglis, I.A., Keramitsoglou, I., Kourtidis, K., 2013. Numerical study of the urban heat island over Athens (Greece) with the WRF model. *Atmos. Environ.* 73, 103–111. <https://doi.org/10.1016/j.atmosenv.2013.02.055>.
- Grell, G.A., Dévényi, D., 2002. A generalized approach to parameterizing convection combining ensemble and data assimilation techniques. *Geophys. Res. Lett.* 29, 10–13. <https://doi.org/10.1029/2002GL015311>.
- Grell, G.A., Peckham, S.E., Schmitz, R., McKeen, S.A., Frost, G., Skamarock, W.C., Eder, B., 2005a. Fully coupled “online” chemistry within the WRF model. *Atmos. Environ.* 39, 6957–6975. <https://doi.org/10.1016/j.atmosenv.2005.04.027>.
- Grell, G.A., Peckham, S.E., Schmitz, R., McKeen, S.A., Frost, G., Skamarock, W.C., Eder, B., 2005b. Fully coupled “online” chemistry within the WRF model. *Atmos. Environ.* 39, 6957–6975. <https://doi.org/10.1016/j.atmosenv.2005.04.027>.
- Guenther, A.B., Jiang, X., Heald, C.L., Sakulyanontvittaya, T., Duhl, T., Immons, L.K., Wang, X., 2012. The model of emissions of gases and aerosols from nature version 2.1 (MEGAN2.1): an extended and updated framework for modeling biogenic emissions. *Geosci. Model Dev.* 5, 1471–1492. <https://doi.org/10.5194/gmd-5-1471-2012>.
- Han, W., Li, Z., Wu, F., Zhang, Y., Guo, J., Su, T., Cribb, M., Fan, J., Chen, T., Wei, J., Lee, S.S., 2020. The mechanisms and seasonal differences of the impact of aerosols on daytime surface urban heat island effect. *Atmos. Chem. Phys.* 20, 6479–6493. <https://doi.org/10.5194/acp-20-6479-2020>.
- Holmer, B., Eliasson, I., 1999. Urban-rural vapour pressure differences and their role in the development of urban heat islands. *Int. J. Climatol.* 19, 989–1009. [https://doi.org/10.1002/\(SICI\)1097-0088\(199907\)19:9<989::AID-JOC410>3.0.CO;2-1](https://doi.org/10.1002/(SICI)1097-0088(199907)19:9<989::AID-JOC410>3.0.CO;2-1).
- Hong, S.Y., Noh, Y., Dudhia, J., 2006. A new vertical diffusion package with an explicit treatment of entrainment processes. *Mon. Weather Rev.* 134, 2318–2341. <https://doi.org/10.1175/MWR3199.1>.
- Hou, A., Ni, G., Yang, H., Lei, Z., 2013. Numerical analysis on the contribution of urbanization to wind stilling: an example over the greater Beijing metropolitan area. *J. Appl. Meteorol. Climatol.* 52, 1105–1115. <https://doi.org/10.1175/JAMC-D-12-013.1>.
- José, R.S., Pérez, J.L., González, R.M., 2013. Using WRF/UCM and CMAQ mesoscale models with very high resolution over European urban cities. *Fresenius Environ. Bull.* 22, 3815–3822. <https://doi.org/10.1007/978-94-007-7756-9>.
- Karlíký, J., Huszář, P., Nováková, T., Belda, M., Švábik, F., Doubalová, J., Halenka, T., 2020. The “urban meteorology island”: a multi-model ensemble analysis. *Atmos. Chem. Phys.* 20, 15061–15077. <https://doi.org/10.5194/acp-20-15061-2020>.
- Konor, C.S., Boezio, G.C., Mechoso, C.R., Arakawa, A., 2009. Parameterization of PBL processes in an atmospheric general circulation model: description and preliminary assessment. *Mon. Weather Rev.* 137, 1061–1082. <https://doi.org/10.1175/2008MWR2464.1>.
- Lee, D.O., 1991. Urban–rural humidity differences in London. *Int. J. Climatol.* 11, 577–582. <https://doi.org/10.1002/joc.3370110509>.
- Li, B., Lu, L., Shi, X., Ma, L., Jiang, J.P., Yabo, S.D., Wang, K., Qi, H., 2023. Drivers of 2015–2021 trends in cold winter surface PM2.5 in the Harbin-Changchun megalopolis in China: meteorology vs. anthropogenic emission. *Atmos. Res.* 285 <https://doi.org/10.1016/j.atmosres.2023.106623>.
- Li, H., Meier, F., Lee, X., Chakraborty, T., Liu, J., Schaap, M., Sodoudi, S., 2018. Interaction between urban heat island and urban pollution island during summer in Berlin. *Sci. Total Environ.* 636, 818–828. <https://doi.org/10.1016/j.scitotenv.2018.04.254>.
- Li, H., Sodoudi, S., Liu, J., Tao, W., 2020. Temporal variation of urban aerosol pollution island and its relationship with urban heat island. *Atmos. Res.* 241, 104957 <https://doi.org/10.1016/j.atmosres.2020.104957>.
- Li, J., Han, Z., 2016. A modeling study of severe winter haze events in Beijing and its neighboring regions. *Atmos. Res.* 170, 87–97. <https://doi.org/10.1016/j.atmosres.2015.11.009>.
- Li, J., Chen, H., Li, Z., Wang, P., Cribb, M., Fan, X., 2015. Low-level temperature inversions and their effect on aerosol condensation nuclei concentrations under different large-scale synoptic circulations. *Adv. Atmos. Sci.* 32, 898–908. <https://doi.org/10.1007/s00376-014-4150-z>.
- Li, M., Wang, T., Xie, M., Zhuang, B., Li, S., Han, Y., Chen, P., 2017b. Impacts of aerosol-radiation feedback on local air quality during a severe haze episode in Nanjing megacity, eastern China. *Tellus Ser. B Chem. Phys. Meteorol.* 69, 1–16. <https://doi.org/10.1080/16000889.2017.1339548>.
- Li, Z., 1998. Influence of absorbing aerosols on the inference of solar surface radiation budget and cloud absorption. *J. Clim.* 11, 5–17. [https://doi.org/10.1175/1520-0442\(1998\)011<0005:IOAAOT>2.0.CO;2](https://doi.org/10.1175/1520-0442(1998)011<0005:IOAAOT>2.0.CO;2).
- Li, Z., Guo, J., Ding, A., Liao, H., Liu, J., Sun, Y., Wang, T., Xue, H., Zhang, H., Zhu, B., 2017a. Special topic: air pollution and control aerosol and boundary-layer

- interactions and impact on air quality. *Natl. Sci. Rev.* 4, 810–833. <https://doi.org/10.1093/nsr/nwx117/4191281>.
- Lin, Y.-L., Farley, R.D., Orville, H.D., 1983. Bulk parameterization of the snow field in a cloud model. *Am. Meteorol. Soc.* 22, 1065–1092.
- Liu, W., You, H., Dou, J., 2009. Urban-rural humidity and temperature differences in the Beijing area. *Theor. Appl. Climatol.* 96, 201–207. <https://doi.org/10.1007/s00704-008-0024-6>.
- Makar, P.A., Gong, W., Hogrefe, C., Zhang, Y., Curci, G., Žabkar, R., Milbrandt, J., Im, U., Balzarini, A., Baró, R., Bianconi, R., Cheung, P., Forkel, R., Gravel, S., Hirtl, M., Honzak, L., Hou, A., Jiménez-Guerrero, P., Langer, M., Moran, M.D., Pabla, B., Pérez, J.L., Pirovano, G., San José, R., Tuccella, P., Werhahn, J., Zhang, J., Galmarini, S., 2015a. Feedbacks between air pollution and weather, part 2: Effects on chemistry. *Atmos. Environ.* 115, 499–526. <https://doi.org/10.1016/j.atmosenv.2014.10.021>.
- Makar, P.A., Gong, W., Milbrandt, J., Hogrefe, C., Zhang, Y., Curci, G., Žabkar, R., Im, U., Balzarini, A., Baró, R., Bianconi, R., Cheung, P., Forkel, R., Gravel, S., Hirtl, M., Honzak, L., Hou, A., Jiménez-Guerrero, P., Langer, M., Moran, M.D., Pabla, B., Pérez, J.L., Pirovano, G., San José, R., Tuccella, P., Werhahn, J., Zhang, J., Galmarini, S., 2015b. Feedbacks between air pollution and weather, part 1: effects on weather. *Atmos. Environ.* 115, 442–469. <https://doi.org/10.1016/j.atmosenv.2014.12.003>.
- Mlawer, E.J., Taubman, S.J., Brown, P.D., Iacono, M.J., Clough, S.A., 1997. Radiative transfer for inhomogeneous atmospheres: RRTM, a validated correlated-k model for the longwave. *J. Geophys. Res. Atmos.* 102, 16663–16682. <https://doi.org/10.1029/97jd00237>.
- Morichetti, M., Madronich, S., Passerini, G., Rizza, U., Mancinelli, E., Virgili, S., Barth, M., 2022. Comparison and evaluation of updates to WRF-Chem (v3.9) biogenic emissions using MEGAN. *Geosci. Model Dev.* 15, 6311–6339. <https://doi.org/10.5194/gmd-15-6311-2022>.
- NCAR Command Language (Version 6.6.2) [Software], 2019. Boulder, Colorado: UCAR/NCAR/CISL/TDD. <https://doi.org/10.5065/D6WD3XH5>.
- Oke, T.R., 1982. The energetic basis of the urban heat island. *Q. J. R. Meteorol. Soc.* 108, 1–24. <https://doi.org/10.1002/qj.49710845502>.
- Oke, T.R., 1995. The heat island of the urban boundary layer: characteristics, causes and effects. *Wind Clim. Cities* 81–107. [https://doi.org/10.1007/978-94-017-3686-2\\_5](https://doi.org/10.1007/978-94-017-3686-2_5).
- Oke, T.R., 2006. Towards better scientific communication in urban climate. *Theor. Appl. Climatol.* 84, 179–190. <https://doi.org/10.1007/s00704-005-0153-0>.
- Oliver Ling, H.L., Ting, K.H., Shaharuddin, A., Kadaruddin, A., Yaacob, M.J., 2010. Air quality and human health in urban settlement: case study of Kuala Lumpur city. *CSR 2010–2010 Int. Conf. Sci. Soc. Res.* 510–515. <https://doi.org/10.1109/CSR.2010.5773831>.
- Petäjä, T., Järvi, L., Kerminen, V.M., Ding, A.J., Sun, J.N., Nie, W., Kujansuu, J., Virkkula, A., Yang, X., Fu, C.B., Zilitinkevich, S., Kulmala, M., 2016. Enhanced air pollution via aerosol-boundary layer feedback in China. *Sci. Rep.* 6, 1–6. <https://doi.org/10.1038/srep18998>.
- Quimbayo-duarte, J., Quimbayo-duarte, J.A., 2019. Numerical Modelling of the Stable Atmospheric Boundary Layer over Complex Terrain and Application to Air Quality to Cite this Version: HAL Id: Tel-02164792 Numerical Modelling of the Wintertime Boundary Layer over Complex Terrain and Application to Air.
- Runnalls, K.E., Oke, T.R., 2000. Dynamics and controls of the near-surface heat island of Vancouver, British Columbia. *Phys. Geogr.* 21, 283–304. <https://doi.org/10.1080/02723646.2000.10642711>.
- Schell, B., Ackermann, J.J., Hass, H., Binkowski, F.S., Ebel, A., 2001. Modeling the formation of secondary organic aerosol within a comprehensive air quality model system. *J. Geophys. Res. Atmos.* 106, 28275–28293. <https://doi.org/10.1029/2001JD000384>.
- Seibert, P., Beyrich, F., Gryning, S.E., Joffre, S., Rasmussen, A., Tercier, P., 2002. Chapter 20 Review and intercomparison of operational methods for the determination of the mixing height. *Dev. Environ. Sci.* 1, 569–613. [https://doi.org/10.1016/S1474-8177\(02\)80023-7](https://doi.org/10.1016/S1474-8177(02)80023-7).
- Shi, C., Nduka, I.C., Yang, Y., Huang, Y., Yao, R., Zhang, H., He, B., Xie, C., Wang, Z., Yim, S.H.L., 2020. Characteristics and meteorological mechanisms of transboundary air pollution in a persistent heavy PM<sub>2.5</sub> pollution episode in Central-East China. *Atmos. Environ.* 223, 117239. <https://doi.org/10.1016/j.atmosenv.2019.117239>.
- Shuzhen, Z., Shu Djen, C., Jingchun, Z., 1991. The turbidity island effect in Shanghai urban climate. *Energ. Build.* 16, 657–662. [https://doi.org/10.1016/0378-7788\(91\)90034-Z](https://doi.org/10.1016/0378-7788(91)90034-Z).
- Skamarock, W.C., Klemp, J.B., Dudhia, J.B., Gill, D.O., Barker, D.M., Duda, M.G., Huang, X.-Y., Wang, W., Powers, J.G., 2008. A Description of the Advanced Research WRF Version 3, NCAR Technical Note TN-475+STR. Tech. Rep., p. 13.
- Skamarock, W.C., Klemp, J.B., Dudhia, J., Gill, D.O., Liu, Z., Berner, J., Wang, W., Powers, J.G., Duda, M.G., Barker, D.M., Huang, X.-Y., 2019. A Description of the Advanced Research WRF Version 4, NCAR Tech. Note NCAR/TN-556+STR:145. <https://doi.org/10.5065/1dfh-6p97>.
- Stockwell, W.R., Kirchner, F., Kuhn, M., Seefeld, S., 1997. A new mechanism for regional atmospheric chemistry modeling. *J. Geophys. Res. Atmos.* 102 <https://doi.org/10.1029/97jd00849>.
- Sun, X., Wang, K., Li, B., Zong, Z., Shi, X., Ma, L., Fu, D., Thapa, S., Qi, H., Tian, C., 2020. Exploring the cause of PM<sub>2.5</sub> pollution episodes in a cold metropolis in China. *J. Clean. Prod.* 256 <https://doi.org/10.1016/j.jclepro.2020.120275>.
- Tao, H., Xing, J., Zhou, H., Chang, X., Li, G., Chen, L., Li, J., 2018. Impacts of land use and land cover change on regional meteorology and air quality over the Beijing-Tianjin-Hebei region, China. *Atmos. Environ.* 189, 9–21. <https://doi.org/10.1016/j.atmosenv.2018.06.033>.
- Ulpiani, G., 2021. On the linkage between urban heat island and urban pollution island: three-decade literature review towards a conceptual framework. *Sci. Total Environ.* 751, 141727. <https://doi.org/10.1016/j.scitotenv.2020.141727>.
- Ulpiani, G., Ranzi, G., Santamouris, M., 2021. Local synergies and antagonisms between meteorological factors and air pollution: a 15-year comprehensive study in the Sydney region. *Sci. Total Environ.* 788, 147783. <https://doi.org/10.1016/J.SCITOTENV.2021.147783>.
- Unger, J., 1999. Urban-rural air humidity differences in Szeged, Hungary. *Int. J. Climatol.* 19, 1509–1515. [https://doi.org/10.1002/\(SICI\)1097-0088\(19991115\)19:13<1509::AID-JOC453>3.0.CO;2-P](https://doi.org/10.1002/(SICI)1097-0088(19991115)19:13<1509::AID-JOC453>3.0.CO;2-P).
- Unkăsević, M., Jovanović, O., Popović, T., 2001. Urban-suburban/rural vapour pressure and relative humidity differences at fixed hours over the area of Belgrade city. *Theor. Appl. Climatol.* 68, 67–73. <https://doi.org/10.1007/s007040170054>.
- Wang, D., Jiang, B., Lin, W., Gu, F., 2019. Effects of aerosol-radiation feedback and topography during an air pollution event over the North China Plain during December 2017. *Atmos. Pollut. Res.* 10, 587–596. <https://doi.org/10.1016/j.apr.2018.10.006>.
- Wang, K., Zhang, Y., Yahya, K., Wu, S.Y., Grell, G., 2015. Implementation and initial application of new chemistry-aerosol options in WRF-Chem for simulating secondary organic aerosols and aerosol indirect effects for regional air quality. *Atmos. Environ.* 115, 716–732. <https://doi.org/10.1016/j.atmosenv.2014.12.007>.
- Wang, Y., Xue, Y., Tian, H., Gao, J., Chen, Y., Zhu, C., Liu, H., Wang, K., Hu, S., Liu, S., Shao, P., 2017. Effectiveness of temporary control measures for lowering PM<sub>2.5</sub> pollution in Beijing and the implications. *Atmos. Environ.* 157, 75–83. <https://doi.org/10.1016/j.atmosenv.2017.03.017>.
- Wild, O., Zhu, X., Prather, M.J., 2000. Fast-J: Accurate simulation of in- and below-cloud photolysis in tropospheric chemical models. *J. Atmos. Chem.* 37, 245–282. <https://doi.org/10.1023/A:1006415919030>.
- Wu, H., Wang, T., Wang, Q., Cao, Y., Qu, Y., Nie, D., 2021. Radiative effects and chemical compositions of fine particles modulating urban heat island in Nanjing, China. *Atmos. Environ.* 247, 118201. <https://doi.org/10.1016/j.atmosenv.2021.118201>.
- Wu, J., Bei, N., Hu, B., Liu, S., Zhou, M., Wang, Q., Li, X., Liu, L., Feng, T., Liu, Z., Wang, Y., Cao, J., Tie, X., Wang, J., Molina, L.T., Li, G., 2019. Aerosol-radiation feedback deteriorates the wintertime haze in the North China Plain. *Atmos. Chem. Phys.* 19, 8703–8719. <https://doi.org/10.5194/acp-19-8703-2019>.
- Xiao, Q., Zheng, Y., Geng, G., Chen, C., Huang, X., Che, H., Zhang, X., He, K., Zhang, Q., 2021. Separating emission and meteorological contributions to long-term PM<sub>2.5</sub> trends over eastern China during 2000–2018. *Atmos. Chem. Phys.* 21, 9475–9496. <https://doi.org/10.5194/acp-21-9475-2021>.
- Yabo, S.D., Fu, D., Li, B., Shi, X., Thapa, S., Shengjin, X., Lu, L., Qi, H., Zhang, W., 2022. Impact of land cover transformation on urban heat islands in Harbin, China. *Environ. Monit. Assess.* 194 <https://doi.org/10.1007/s10661-022-10066-z>.
- Yabo, S.D., Fu, D., Li, B., Ma, L., Shi, X., Lu, L., Shengjin, X., Meng, F., Jiang, J., Zhang, W., Qi, H., 2023. Synergistic interactions of fine particles and radiative effects in modulating urban heat islands during winter haze event in a cold megacity of Northeast China. *Environ. Sci. Pollut. Res.* <https://doi.org/10.1007/s11356-023-26636-8>.
- Yang, G., Ren, G., Zhang, P., Xue, X., Tysa, S.K., Jia, W., Qin, Y., Zheng, X., Zhang, S., 2021. PM<sub>2.5</sub> influence on urban heat island (UHI) effect in Beijing and the possible mechanisms. *J. Geophys. Res. Atmos.* 126, 1–25. <https://doi.org/10.1029/2021JD035227>.
- Yang, P., Ren, G., Hou, W., 2017. Temporal-spatial patterns of relative humidity and the urban dryness island effect in Beijing City. *J. Appl. Meteorol. Climatol.* 56, 2221–2237. <https://doi.org/10.1175/JAMC-D-16-0338.1>.
- Yang, P., Ren, G., Yan, P., Deng, J., 2020a. Temporal-spatial pattern of surface wind speed and the “Urban Stilling Island” in Beijing City. *J. Meteorol. Res.* 34, 986–996. <https://doi.org/10.1007/s13351-020-9135-5>.
- Yang, X., Zhao, C., Guo, J., Wang, Y., 2016. Intensification of aerosol pollution associated with its feedback with surface solar radiation and winds in Beijing. *J. Geophys. Res.* 121, 4093–4099. <https://doi.org/10.1002/2015JD024645>.
- Yang, Y., Zheng, Z., Yim, S.Y.L., Roth, M., Ren, G., Gao, Z., Wang, T., Li, Q., Shi, C., Ning, G., Li, Y., 2020b. PM<sub>2.5</sub> pollution modulates wintertime urban heat island intensity in the Beijing-Tianjin-Hebei Megalopolis, China. *Geophys. Res. Lett.* 47, 3. <https://doi.org/10.1029/2019GL084288>.
- Yu, H., Liu, S.C., Dickinson, R.E., 2002. Radiative effects of aerosols on the evolution of the atmospheric boundary layer. *J. Geophys. Res. Atmos.* 107 <https://doi.org/10.1029/2001jd000754>.
- Zhang, Y., Van Vu, T., Sun, J., He, J., Shen, X., Lin, W., Zhang, X., Zhong, J., Gao, W., Wang, Y., Fu, T.M., Ma, Y., Li, W., Shi, Z., 2020. Significant changes in chemistry of fine particles in wintertime Beijing from 2007 to 2017: impact of clean air actions. *Environ. Sci. Technol.* 54, 1344–1352. <https://doi.org/10.1021/acs.est.9b04678>.
- Zheng, G.J., Duan, F.K., Su, H., Ma, Y.L., Cheng, Y., Zheng, B., Zhang, Q., Huang, T., Kimoto, T., Chang, D., Pöschl, U., Cheng, Y.F., He, K.B., 2015. Exploring the severe winter haze in Beijing: the impact of synoptic weather, regional transport and heterogeneous reactions. *Atmos. Chem. Phys.* 15, 2969–2983. <https://doi.org/10.5194/acp-15-2969-2015>.
- Zhou, S.Z., 1994. Discussion of the urban-rural differences in atmospheric humidity of Shanghai area. *Trans. Oceanol. Limnol.* 2, 13–25.